

Article

Simulation of the Dynamic Responses of Layered Polymer Composites under Plate Impact Using the DSGZ Model

Huadian Zhang ¹, Arunachalam M. Rajendran ¹, Manoj K. Shukla ², Sasan Nouranian ^{3,4}, Ahmed Al-Ostaz ^{4,5}, Steven Larson ² and Shan Jiang ^{1,*}

¹ Department of Mechanical Engineering, University of Mississippi, University, MS 38677, USA; hzhang10@go.olemiss.edu (H.Z.); raj@olemiss.edu (A.M.R.)

² Environmental Laboratory, U.S. Army Engineering Research and Development Center, Vicksburg, MS 39180, USA; manoj.k.shukla@erdc.dren.mil (M.K.S.); steven.l.larson@usace.army.mil (S.L.)

³ Department of Chemical Engineering, University of Mississippi, University, MS 38677, USA; sasan@olemiss.edu

⁴ Center for Graphene Research and Innovation, University of Mississippi, University, MS 38677, USA; alostaz@olemiss.edu

⁵ Department of Civil Engineering, University of Mississippi, University, MS 38677, USA

* Correspondence: jiang@olemiss.edu

Abstract: This paper presents a numerical study on the dynamic response and impact mitigation capabilities of layered ceramic–polymer–metal (CPM) composites under plate impact loading, focusing on the layer sequence effect. The layered structure, comprising a ceramic for hardness and thermal resistance, a polymer for energy absorption, and a metal for strength and ductility, is analyzed to evaluate its effectiveness in mitigating the impact loading. The simulations employed the VUMAT subroutine of DSGZ material models within Abaqus/Explicit to accurately represent the mechanical behavior of the polymeric materials in the composites. The VUMAT implementation incorporates the explicit time integration scheme and the implicit radial return mapping algorithm. A safe-version Newton–Raphson method is applied for numerically solving the differential equations of the J_2 plastic flow theory. Analysis of the simulation results reveals that specific layer configurations significantly influence wave propagation, leading to variations in energy absorption and stress distribution within the material. Notably, certain layer sequences, such as P-C-M and C-P-M, exhibit enhanced impact mitigation with a superior ability to dissipate and redirect the impact energy. This phenomenon is tied to the interactions between the material properties of the ceramic, polymer, and metal, emphasizing the necessity of precise material characterization and enhanced understanding of the layer sequencing effect for optimizing composite designs for impact mitigation. The integration of empirical data with simulation methods provides a comprehensive framework for optimizing composite designs in high-impact scenarios. In the general fields of materials science and impact engineering, the current research offers some guidance for practical applications, underscoring the need for detailed simulations to capture the high-strain-rate dynamic responses of multilayered composites.

Keywords: layered ceramic–polymer–metal composites; plate impact simulation; stress wave propagation; finite element method; Abaqus; VUMAT



Citation: Zhang, H.; Rajendran, A.M.; Shukla, M.K.; Nouranian, S.; Al-Ostaz, A.; Larson, S.; Jiang, S. Simulation of the Dynamic Responses of Layered Polymer Composites under Plate Impact Using the DSGZ Model. *J. Compos. Sci.* **2024**, *8*, 159. <https://doi.org/10.3390/jcs8050159>

Academic Editor: Zhong Hu

Received: 26 February 2024

Revised: 12 April 2024

Accepted: 19 April 2024

Published: 23 April 2024



Copyright: © 2024 by the authors. Licensee MDPI, Basel, Switzerland. This article is an open access article distributed under the terms and conditions of the Creative Commons Attribution (CC BY) license (<https://creativecommons.org/licenses/by/4.0/>).

1. Introduction

Layered polymer composites are a type of engineered material that possesses exceptional mechanical properties, including high strength-to-weight ratios, tailored stiffness, and enhanced impact resistance [1]. These materials have a multilayered architecture that is designed to dissipate energy and mitigate the effects of both low- and high-speed impacts, resulting in their unique properties [2,3]. The propagation of stress waves, including shock waves, through composite materials is a crucial aspect of materials science

and engineering. This propagation provides insights into material behavior under extreme conditions, aiding in the design of protective equipment, vehicle armor systems, and aerospace components [4]. As technologies have advanced, the demand for lighter, stronger, and more resilient materials has increased. Research has been ongoing for decades on the complex interaction between the mechanical properties of individual layers and their collective response under shock loading [5,6]. Early work in this area, which was largely experimental, focused on the response of homogeneous materials to impact loading. Previous research has investigated the impact resistance of composites created by layering polymers and reinforcing materials [7]. The sequence of layers plays an important role in determining the dynamic response of the composite. Placing harder materials on the impact surface can modify the initial wave characteristics, while designing subsequent layers can absorb and dissipate the remaining energy. Computational tools have greatly improved the simulation of stress wave behavior in layered composites [8,9]. Advances in computational modeling have provided a strong foundation for analyzing the behavior of composites under impact loading. The finite element method (FEM) has been widely used to model the complex interactions within these materials. FEM simulation allows for detailed analysis of stress wave propagation, deformation, and failure mechanisms at a granular level, making it a cornerstone of the field [10]. Researchers have modeled the effects of various parameters, such as layer thickness, material properties, and bonding quality, on the impact resistance of composites. However, a deeper understanding of their effect on the overall performance of layered polymer composites under extreme loading conditions is still needed. Further research is necessary to explore the dynamic responses of composites, including wave interactions at material interfaces, the effect of impedance mismatch across layered structures, and the role of cohesive zone properties in energy absorption. The focus of this research is on optimizing the layer sequence in composite structures for advanced engineering applications. It is a fundamental investigation for the research goals mentioned above.

Polymer materials, such as polycarbonate (PC), polymethyl methacrylate (PMMA), and polyurea, have been shown to improve the performance of layered composite structures under impact loads. Several experiments and simulations indicate that polymeric materials can enhance the impact performance of bi-layer, multi-layer, and coated panels [11–16]. For instance, Tekalur et al. [14] discovered that incorporating a compliant material in a bi-layer composite and between two rigid layers can improve the impact performance by approximately 25 to 100% compared to a single stiff layer. Amini et al. [17] indicated that placing a polymer material on the impact side of a bi-layer composite could reduce its impact performance, unlike when it is on the opposite side. Chu et al. [18] conducted a numerical and experimental analysis to study the effect of polymer coating thickness on strengthening under debris impact. The study found that increasing the coating thickness provided limited improvement in impact resistance due to its erosion-mitigating effect on the polymer/steel structure. However, low-thickness polymer coatings demonstrated an enhanced ability to superimpose wave reflections at the high-impedance polymer/steel interface before energy transfer. Enhanced pressure and instantaneous specific energy density can induce hardening and strengthening within the polymer, alter the failure mode of the steel plate, and improve the impact resistance of the polymer coating.

The accurate numerical prediction of the mechanical behavior of polymer materials under extreme loading conditions depends heavily on the availability of robust constitutive laws that govern the dynamic responses. Numerous studies have analyzed the behavior of polymers subjected to uniaxial compression tests at various strain rates and temperatures [19,20]. The findings reported in the literature consistently reveal that stress increases with higher strain rates and decreases with rising temperatures, indicating a clear dependency of the polymer's deformation behavior on these two factors. These comprehensive studies, covering a wide range of strain rates and temperatures, offer valuable insights for designing products suited to various operational conditions [21]. Several constitutive models [22–26] have been developed to predict the deformation behavior of polymers

under large strains, incorporating both strain softening and strain hardening characteristics. These models establish a constitutive relationship where stress is not solely dependent on strain but is also influenced by strain rate and temperature, as they are derived from compression tests conducted at different strain rates and temperatures. Two primary methods are employed to develop constitutive models that describe the correlation between stress and strain. The physical approach originates from the thermodynamic activation of molecules and is characterized by complex equations [27]. The phenomenological approach, on the other hand, models the stress–strain relationship empirically by fitting experimental data. Due to its simplicity and efficiency, the phenomenological model, which uses curve fitting or machine learning, is favored in numerical simulations to elucidate the behavior of materials [28]. Therefore, it is essential to have a constitutive model that can be integrated into finite element codes to predict the mechanical behavior of materials, including their flow characteristics. For instance, Duodu et al. [29] demonstrated the use of Abaqus FEM software with vectorized user-defined material (VUMAT) to model the responses of layered composites to high-velocity impacts. Their study emphasized the accuracy of FEM in predicting material behavior under such conditions, which is consistent with experimental observations. One such constitutive model developed for glassy and semicrystalline polymers is known as the DSGZ constitutive law, named after the initials of its authors [1]. The DSGZ model characterizes the behavior of specified materials under uniaxial compression loading, with a particular emphasis on the strain softening preceding the strain hardening. For example, Achour et al. [30] and Nahar et al. [31] implemented the DSGZ model in Abaqus with user-defined material (UMAT) and VUMAT, respectively, to model the behavior of polymers under low-to-moderate strain rates. UMAT and VUMAT are FORTRAN subroutines that can be utilized in Abaqus/Standard for quasi-static problems and Abaqus/Explicit for dynamic problems, respectively. Implementing user-defined material in Abaqus typically requires a complete definition of material behavior, including its initial elastic definition, plastic flow characterization, and damage criterion. The most critical aspect of this definition is that of plastic flow, which necessitates the input of a suitable flow law and an effective numerical solution scheme for the corresponding differential equations.

The objective of this study is to predict the mechanical behaviors and dynamic responses of layered polymers in ceramic–polymer–metal (CPM) composites under plate impact loading. To achieve this, we utilized the generalized and modified DSGZ models and the radial return mapping method with a safe-version Newton–Raphson root-finding algorithm within Abaqus/Explicit (2023 version) through VUMAT subroutines. The rest of this paper is organized as follows: Section 2 introduces the fundamental concepts related to the impact dynamics of composites, including the time integration scheme of J_2 flow theory, the formulas of the DSGZ models, the DSGZ VUMAT implementation, some supplementary material models, and a brief overview of 1-D impact dynamics; Section 3 provides details on the modeling and simulations conducted for DSGZ VUMAT subroutine validations, individual layer impact tests, and CPM composite tests; Section 4 presents and discusses the comprehensive results obtained from these tasks. Critical dynamic responses and mechanical behaviors, denoted by nodal velocity and element stress, were investigated for both the CPM composites and the protected target.

2. Numerical Simulation Methods

A comprehensive understanding of transient, nonlinear dynamics problems requires knowledge of the material models that govern the relationships among flow variables, such as pressure, mass density, energy density, temperature, and other relevant parameters. These relationships conventionally incorporate a strength model, an equation of state (EOS), and a failure model dedicated to each constituent in composite structures. These equations stem from the decomposition of the stress tensor into a hydrostatic stress tensor and a deviatoric stress tensor, which, respectively, induce volume changes and govern material deformations. The strength model establishes correlations between the deviatoric stress

tensor and various parameters that characterize the extent and rate of deformation, as well as the influence of temperature. The EOS is employed to establish the relationship between pressure, mass density, and internal energy density. Furthermore, a comprehensive material model typically includes a failure model, which is an equation that describes the stress and/or strain conditions leading to material fracture. Upon reaching these conditions, the material loses its capability to withstand normal and shear stresses. Considering the scope of this study, which does not explore dynamic tensile failure, our focus has been solely on examining the strength model and EOS. Similarly, since the impact loading conditions in this study typically do not involve significant thermal radiation or energy dissipation, the effect of temperature was not considered.

The analysis of transient nonlinear dynamics problems, such as the interaction of objects during stress wave propagation, requires the simultaneous solution of governing partial differential equations that capture mass, momentum, and energy conservation, incorporating material constitutive laws and rigorously defined initial and boundary conditions. Resolving these equations typically involves numerical methods that use a second-order, accurate, explicit scheme. Specifically, the Lagrange method is used for solids that undergo less motion and deformation. Due to the exclusive use of Abaqus/Explicit in this work, versatile commercial software that is well designed for transient, nonlinear analysis within the scope of general-purpose numerical simulations, the required conditions of the conservation equations and native support (built-in) constitutive laws are inherently satisfied. Consequently, a comprehensive numerical solution procedure is required for implementing the VUMAT of the generalized and modified DSGZ constitutive laws based on J_2 flow theory, as outlined in Sections 2.1–2.3. In addition, we briefly present several constitutive laws for non-polymeric materials in Section 2.4, apart from DSGZ models, emphasizing their unique characteristics. Section 2.5 explains the initiation and propagation of stress waves in terms of impact-induced velocity and stress.

2.1. Time Integration Scheme of the J_2 Flow Theory

Finite difference methods-based time integration algorithms are widely used in the finite element analysis of mechanics-related problems. These algorithms discretize time on a finite grid, where the interval between consecutive grid points represents the time step Δt . The integration scheme calculates the corresponding quantities at a future time $t + \Delta t$, using the positions and specific time derivatives at the current time t . This iterative process enables the tracking of the temporal evolution of these quantities. To implement numerical discretization and time integration in J_2 flow theory, we next provide brief overviews of J_2 plasticity, the radial return mapping method, and root-finding algorithms.

The complete description of J_2 plasticity, commonly referred to as the von Mises yield criterion, was introduced by Huber and Mises a century ago [32,33]. This plastic model has found widespread application in the fields of mechanical engineering and materials science. It assumes a scalar yield function f expressed as

$$f = \bar{\sigma} - \sigma_y(\bar{\epsilon}^p, \dot{\bar{\epsilon}}^p, T) = 0, \tag{1}$$

where $\bar{\sigma}$ is the von Mises equivalent stress, or effective stress, defined from the deviatoric stress tensor $\sigma^d = \sigma - \frac{1}{3} \cdot \text{tr}[\sigma] \cdot I$ as

$$\bar{\sigma} = \sqrt{\frac{3}{2} \sigma^d : \sigma^d}, \tag{2}$$

and σ_y is the so-called current yield stress of the material. Typically, the yield stress defined by the flow law depends on the equivalent plastic strain $\bar{\epsilon}^p$, equivalent plastic strain rate $\dot{\bar{\epsilon}}^p$, and temperature T , which are given by

$$\bar{\epsilon}^p = \int_0^t \dot{\bar{\epsilon}}^p dt = \int_0^t \sqrt{\frac{2}{3} \dot{\epsilon}^p : \dot{\epsilon}^p} dt \tag{3}$$

and

$$\dot{T} = \frac{\eta}{\rho \cdot C_p} \sigma : \dot{\epsilon}_{ij}, \tag{4}$$

where $\dot{\epsilon}^p = \dot{\epsilon}_{ij}$ is the plastic part of the deformation gradient tensor, η is the Taylor–Quinney [34] latent coefficient converting the amount of plastic work into heat energy, and C_p is the specific heat. In the realm of J_2 plasticity, the yield function f delineates the boundary of the elastic region ($f < 0$) and the yield surface ($f = 0$). Meanwhile, the deviated stress value is corrected by the radial return mapping method ($f > 0$). The plastic flow direction is determined by the flow rule, where the plastic deformation gradient can be expressed with $\dot{\epsilon}^p = \gamma \cdot \hat{n}$, where γ is the flow intensity, and \hat{n} represents the flow direction with $\hat{n} = \sigma^d / \sqrt{\sigma^d : \sigma^d}$ (the unit normal to the flow stress determined exclusively in terms of the trial elastic stress in the radial return mapping method). Hence, the form of the equivalent plastic strain becomes

$$\bar{\epsilon}^p = \int_0^t \dot{\epsilon}^p dt = \int_0^t \sqrt{\frac{2}{3}} \gamma dt = \sqrt{\frac{2}{3}} \Gamma. \tag{5}$$

To implement the plasticity model described above into a numerical simulation, the rate constitutive equations need to be integrated appropriately with respect to an incremental objective algorithm. A widely employed approach for the time integration of the J_2 plasticity with isotropic hardening is the radial return mapping algorithm [35,36], which has been extensively documented and detailed in numerous publications [32,37,38]. The core of the radial return mapping algorithm is the trial stress calculated from the fully elastic model. Numerically, the strain increment between the current time step (t_0) and the next time step (t_1) is defined as $\Delta\epsilon$, and the deviatoric stress tensor at the current time step is defined as S_0^d . At the beginning of the current time step, the deviatoric trial stress tensor S_{tr}^d and the hydrostatic pressure p_1 for the next time step are calculated via the elastic law, so that

$$S_{tr}^d = S_0^d + 2 \cdot G \cdot \Delta\epsilon^d \tag{6}$$

and

$$p_1 = p_0 + K \cdot tr[\Delta\epsilon], \tag{7}$$

where G is the shear modulus, K is the bulk modulus, and $\Delta\epsilon^d$ is the deviatoric strain increment. Conforming to Equation (1), the yield function at the next time step is therefore

$$f = \bar{\sigma}_{tr} - \sigma_y^0(\bar{\epsilon}_0^p, \dot{\epsilon}_0^p, T_0) = 0, \tag{8}$$

with $\bar{\sigma}_{tr} = \sqrt{\frac{3}{2} \cdot S_{tr}^d : S_{tr}^d}$, which is defined from Equation (2), and σ_y^0 is the equilibrated yield stress of the previous increment. By examining the sign of the yield function, the admissibility of the trial stress can be determined. If $f \leq 0$, the current increment is entirely elastic, and the predicted stress is admissible, resulting in a final stress value $S_1^d = S_{tr}^d$; however, if $f > 0$, the trial stress is deemed inadmissible, necessitating a plastic correction of the final stress value S_1^d . The plastic correction is computed by enforcing Equation (8) with respect to the generalized consistency parameter $\Gamma = \int_0^t \gamma dt$, defined in Equation (5), at the end of the current increment in the form of

$$f(\Gamma) = \sqrt{\frac{3}{2} S_1^d : S_1^d} - \sigma_y^1(\bar{\epsilon}_1^p, \dot{\epsilon}_1^p, T_1) = 0, \tag{9}$$

with

$$\begin{cases} S_1 = S_{tr} - 2 \cdot G \cdot \Gamma \cdot |\hat{n}| \\ \bar{\epsilon}_1^p = \bar{\epsilon}_0^p + \sqrt{\frac{3}{2}} \Gamma \\ \dot{\bar{\epsilon}}_1^p = \frac{1}{\Delta t} \cdot \sqrt{\frac{3}{2}} \Gamma \\ T_1 = T_0 + \frac{\eta}{\rho \cdot C_p} \cdot (\sigma_y^0 + \sigma_y^1) \sqrt{\frac{3}{2}} \Gamma \end{cases} \quad (10)$$

Such an expression can then be simplified as

$$f(\Gamma) = \bar{\sigma}_{tr} - \sqrt{6} \cdot G \cdot \Gamma - \sigma_y^1(\Gamma) = 0, \quad (11)$$

and leaves only one unknown value of Γ .

In this study, we adopted the so-called root-finding method introduced by Zaera et al. [39]. Such an approach has been enhanced by Ming et al. [40] to implicitly solve the yield function (Equation (11)) through the radial return mapping algorithm. In their study, the safe version of the Newton–Raphson method was developed. The “safe” term is attributed to the integrated bisection method, which serves as a supplementary process when necessary, exhibiting the balance between efficiency and precision. The Newton–Raphson method [41] stands out as the most well-known approach for finding roots in nonlinear equations, owing to its simplicity and efficiency. Its primary limitation lies in the requirement to evaluate the derivative $f'(x)$ of the function $f(x)$. Consequently, its applicability is restricted to situations where $f'(x)$ can be easily computed or numerically evaluated. By expanding the Taylor series of $f(x)$ around the point x , a more accurate approximation can be derived in the expression of $x_{i+1} = x_i - f(x)/f'(x)$. The Newton–Raphson method involves an iterative process, initiated with a first guessing x_0 for a root of the function $f(x)$, and the process continues until the convergence criterion, as given by $|x_{i+1} - x_i| \leq \epsilon_{NR}$, where ϵ_{NR} is the tolerance of the Newton–Raphson method, is reached. In certain situations, the Newton–Raphson method may exhibit poor or no global convergence due to the tangent line not always approximating the function and the non-differentiable point x_s in a piecewise function $f(x)$ defined by two different expressions on the left and right sides. Therefore, the safe version of the Newton–Raphson method was proposed to combine the Newton–Raphson and bisection methods [40]. The key innovation of this method lies in the termination of the Newton–Raphson iteration when the result accidentally moves out of the root-finding interval $[x_0, x_1]$ such that $f(x_0) \cdot f(x_1) < 0$. At this point, bisection gets involved to reposition the initial guess to be $x = x_0 + \frac{1}{2} \cdot (x_1 - x_0)$, thereby facilitating the continuation of the Newton–Raphson algorithm. In case of Equation (11), the application of the Newton–Raphson method requires the calculation of the derivative $f'(\Gamma)$ of the yield function $f(\Gamma)$ with respect to the Γ parameter, so that

$$f'(\Gamma) = -\sqrt{6} \cdot G - \frac{d\sigma_y(\Gamma)}{d\Gamma}, \quad (12)$$

with the definition for the derivative of the yield stress function with respect to Γ as

$$\frac{d\sigma_y(\Gamma)}{d\Gamma} = \sqrt{\frac{2}{3}} \cdot \left(\frac{\partial \sigma_y}{\partial \bar{\epsilon}^p} + \frac{1}{\Delta t} \cdot \frac{\partial \sigma_y}{\partial \dot{\bar{\epsilon}}^p} + \frac{\eta \cdot \sigma_y}{\rho \cdot C_p} \frac{\partial \sigma_y}{\partial T} \right). \quad (13)$$

A conventional approach for computing the derivatives of the yield stress function $\sigma_y(\Gamma)$, concerning the variables $\bar{\epsilon}^p$, $\dot{\bar{\epsilon}}^p$, and T , involves employing an analytical method. This method entails determining the analytical expression for each partial derivative based on the hardening flow law of the material. However, obtaining derivatives through the analytical method can be a challenge for many yield functions. Therefore, in such instances, a numerical solution, namely the finite difference method, is used alternatively. This numerical solution entails introducing a small increment to $\bar{\epsilon}^p$, $\dot{\bar{\epsilon}}^p$, and T , respectively.

Subsequently, the three partial derivatives of σ_y with respect to $\bar{\epsilon}^p, \bar{\dot{\epsilon}}^p$, and T in Equation (13) can be computed, and they can be expressed as

$$\frac{\partial \sigma_y}{\partial \bar{\epsilon}^p} = \frac{\sigma_y(\bar{\epsilon}^p + \Delta \bar{\epsilon}^p, \bar{\dot{\epsilon}}^p, T) - \sigma_y(\bar{\epsilon}^p, \bar{\dot{\epsilon}}^p, T)}{\Delta \bar{\epsilon}^p}, \tag{14}$$

$$\frac{\partial \sigma_y}{\partial \bar{\dot{\epsilon}}^p} = \frac{\sigma_y(\bar{\epsilon}^p, \bar{\dot{\epsilon}}^p + \Delta \bar{\dot{\epsilon}}^p, T) - \sigma_y(\bar{\epsilon}^p, \bar{\dot{\epsilon}}^p, T)}{\Delta \bar{\dot{\epsilon}}^p}, \tag{15}$$

and

$$\frac{\partial \sigma_y}{\partial T} = \frac{\sigma_y(\bar{\epsilon}^p, \bar{\dot{\epsilon}}^p, T + \Delta T) - \sigma_y(\bar{\epsilon}^p, \bar{\dot{\epsilon}}^p, T)}{\Delta T}. \tag{16}$$

The stability of the solving process and the accuracy of the results depend on the correct choice for these increments. In this work, these increments were fixed at a value of 10^{-8} , which was considered a small enough time step for sensitivity concerns, as reported by Neto et al. [42].

2.2. The DSGZ Models

To describe the stress–strain curves for glassy and semicrystalline polymers, the phenomenological DSGZ constitutive law [23] was developed by integrating four distinct constitutive models, namely Johnson–Cook [43], G’Sell Jonas [22], Matsuoka [44], and Brooks [45]. The yield stress equation of the standard DSGZ model for uniaxial compression has a form of

$$\sigma_y(\epsilon, \dot{\epsilon}, T) = K \cdot \{f(\epsilon) + [q(\dot{\epsilon}, T) - f(\epsilon)] \cdot r(\dot{\epsilon}, T)\} \cdot h(\dot{\epsilon}, T), \tag{17}$$

where $f(\epsilon), h(\dot{\epsilon}, T), q(\dot{\epsilon}, T)$, and $r(\dot{\epsilon}, T)$ components are

$$f(\epsilon) = (e^{-C_1 \cdot \epsilon} + \epsilon^{C_2}) \cdot (1 - e^{-\alpha \cdot \epsilon}), \tag{18}$$

$$h(\dot{\epsilon}, T) = \dot{\epsilon}^m \cdot e^{\frac{a}{T}}, \tag{19}$$

$$q(\dot{\epsilon}, T) = \frac{\epsilon \cdot e^{(1 - \frac{\epsilon}{C_3 \cdot h(\dot{\epsilon}, T)})}}{C_3 \cdot h(\dot{\epsilon}, T)}, \tag{20}$$

and

$$r(\dot{\epsilon}, T) = e^{(\ln(g(\dot{\epsilon}, T) - C_4) - C_4) \cdot \epsilon}, \tag{21}$$

where $\sigma_y, \epsilon, \dot{\epsilon}$, and T are true stress (at yield surface), true strain, true strain rate, and absolute temperature, respectively; $K, C_1, C_1, C_1, a, \alpha$, and m are the material parameters; $f(\epsilon)$ denotes the deformation due to strain hardening; $g(\dot{\epsilon}, T)$ is defined to be the dimensionless form of $h(\dot{\epsilon}, T)$, representing the dependency of stress and deformation on strain rate and temperature; $q(\dot{\epsilon}, T)$ describes the shift behavior of yield point with varying strain rate and temperature; and $r(\dot{\epsilon}, T)$ depicts the exponential evolution of stress from the initial value to the steady state value. For a more in-depth exploration of the formulation of the standard DSGZ equation and the process of material parameter calibration, readers are referred to [23].

For some polymeric materials whose uniaxial tension and compression properties deviate, the effect of hydrostatic pressure becomes a necessary factor in accurately characterizing their mechanical behavior. Thus, a generalized DSGZ model [46] was proposed to describe the stress–strain relationship of polymers under any loading mode and is presented by equation

$$\bar{\sigma}_y(\bar{\epsilon}, \bar{\dot{\epsilon}}, T, p) = \bar{\sigma}_y(\bar{\epsilon}, \bar{\dot{\epsilon}}, T) - \gamma p, \tag{22}$$

where γ is hydrostatic coefficient, p is hydrostatic pressure, and $\bar{\sigma}_y(\bar{\epsilon}, \dot{\bar{\epsilon}}, T)$ is given by Equation (17) by denoting the equivalent stress $\bar{\sigma}_y$ for σ_y and substituting equivalent strain $\bar{\epsilon}$ for ϵ and equivalent strain rate $\dot{\bar{\epsilon}}$ for $\dot{\epsilon}$. Specifically, the equivalent stress equation can be divided into two parts, which are in the form of

$$\bar{\sigma}_y^t(\bar{\epsilon}, \dot{\bar{\epsilon}}, T) = \frac{1}{1 + \frac{\gamma}{3}} \cdot \bar{\sigma}_y(\bar{\epsilon}, \dot{\bar{\epsilon}}, T) \tag{23}$$

and

$$\bar{\sigma}_y^c(\bar{\epsilon}, \dot{\bar{\epsilon}}, T) = \frac{1}{1 - \frac{\gamma}{3}} \cdot \bar{\sigma}_y(\bar{\epsilon}, \dot{\bar{\epsilon}}, T), \tag{24}$$

for a uniaxial tension test and a uniaxial compression test, respectively.

Because of the weak prediction of high-strain deformation, many researchers have proposed a modified version of the standard DSGZ model. For example, Dar et al. [47] utilized a model that has two variants in describing the initial elastic and yield stress shift behavior. Their model aimed at resolving the issue when simulating the high-strain-rate deformation. Hence, material parameters for the modified DSGZ model usually have two sets, one for a low strain rate and one for a high strain rate, since they both have discrepancies in predicting stress–strain behaviors. The yield stress equation of the modified DSGZ model has the same form as that in Equation (20), while $f(\epsilon)$ and $q(\dot{\epsilon}, T)$ components have different expressions as

$$f(\epsilon) = (e^{C_0 \cdot \epsilon} + \epsilon^{C_1} - C_2) \cdot (1 - e^{-\alpha \cdot \epsilon}) \tag{25}$$

and

$$q(\dot{\epsilon}, T) = \frac{\epsilon \cdot e^{(1 - \frac{\epsilon}{C_2 \cdot h(\dot{\epsilon}, T)})}}{C_3 \cdot h(\dot{\epsilon}, T)}, \tag{26}$$

where C_0 is the newly introduced parameter. In the modified DSGZ model, the hydrostatic coefficient γ is depreciated.

2.3. VUMAT Implementation

Herein, the VUMAT implementation with a FORTRAN subroutine includes the radial return mapping algorithm for solving J_2 plasticity within the framework of the DSGZ constitutive laws. This section provides a concise overview of our VUMAT implementation, with the schematic flowchart depicted in Figure 1. The initial block of the flowchart is dedicated to obtaining the material properties, which are defined as user material constants. Abaqus/Explicit provides the VUMAT subroutine with the following quantities: the strain increment $\Delta\epsilon$ for the current time step; the stress tensor σ_0 and the temperature T_0 at the beginning of the current increment; the time increment Δt , corresponding to the current time step; a table of solution-dependent state variables (SDVs) used to store essential data such as $\bar{\epsilon}^p$, $\dot{\bar{\epsilon}}^p$, and Γ , which facilitates data transfer to the next time step. The VUMAT subroutine must compute and return the value of the new stress tensor σ_1 and all SDVs at the end of the increment for each time integration instance. The internal and dissipated energies have also to be evaluated to compute the temperatures in thermal coupling problems.

In the VUMAT subroutine, the “package” module within the Abaqus software requires a mandatory step for establishing the initial values [48], specifically obtaining the accurate time increment Δt based on the elastic material parameters. During the normal VUMAT computation, the trial equivalent stress $\bar{\sigma}_{tr}$, which is calculated from the deviatoric trial stress tensor S_{tr}^d , is compared with the yield stress at the beginning of the increment σ_y^0 to test if the current step is fully elastic or partly plastic. Equations (6) and (7) are adopted for the new deviatoric trial stress tensor S_{tr}^d and hydrostatic pressure p_1 values. If $\bar{\sigma}_{tr} \leq \sigma_y^0$, the element is in the elastic realm, the plastic correction step can be omitted. In this case, the predicted stress S_1^d is S_{tr}^d , the plastic corrector parameter Γ is set to 0,

and the yield stress remains unchanged as $\sigma_y^1 = \sigma_y^0$. If $\bar{\sigma}_{tr} \leq \sigma_y^0$, the element is at least partially plastic, it becomes necessary to compute the plastic corrector parameter Γ to draw back the predicted stress onto the yield surface of the material at the end of the current increment. We employed the safe version of the Newton–Raphson method [40] to perform the plastic correction process. To enhance efficiency, the plastic corrector Γ is initialized to its value at the end of the previous increment as Γ_0 . In the case of the first plastic increment, i.e., $\dot{\epsilon}_0^p = \dot{\epsilon}_0 = 0$, $q(\dot{\epsilon}, T)$ in Equation (20) cannot be calculated. Therefore, a relatively small value of Γ is set to 10^{-8} instead of zero. The initial interval for the bisection method is initialized to $\Gamma \in [0, \bar{\sigma}_{tr} / \sqrt{6} \cdot G]$. The predicted equivalent plastic strain $\dot{\epsilon}_1^p$, plastic strain rate $\dot{\epsilon}_1^p$, and temperature T_0 at the end of the increment are computed via Equation (10). The yield stress σ_y^1 , yield function $f(\Gamma)$, and its derivatives $f'(\Gamma)$ are then obtained. Next, the convergence of the Newton–Raphson method is examined by comparing the Γ parameter increment $\Delta\Gamma = -f(\Gamma) / f'(\Gamma)$ to the Newton–Raphson user-defined precision ϵ_{NR} (10^{-12} in this work). If $\Delta\Gamma > \epsilon_{NR}$, iteration continues with the new Γ parameter value of $\Gamma = \Gamma + \Delta\Gamma$ until $\Delta\Gamma \leq \epsilon_{NR}$. Thus, the final S_1^d is drawn back on the yield surface by $S_1^d = S_{tr} - 2 \cdot G \cdot \Gamma \cdot \bar{n}$ with $\bar{n} = S_{tr} / \sqrt{S_{tr} : S_{tr}}$. Finally, all necessary variables are updated to SDVs for the next strain increment.

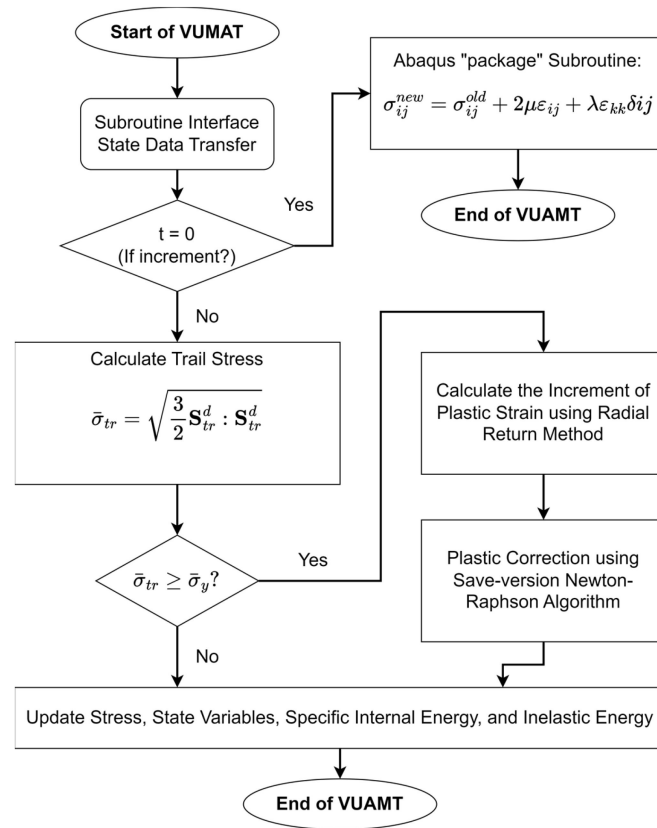


Figure 1. Flowchart of the VUMAT implementation.

In addition, during the VUMAT subroutine calculation of $f'(\Gamma)$ in Equation (13), the derivatives of the yield stress function σ_y in Equation (17) for the standard DSGZ model with respect to ϵ , $\dot{\epsilon}$, and T can be expressed as

$$\frac{\partial \sigma_y}{\partial \epsilon} = K \cdot \left[\frac{\partial f}{\partial \epsilon} + \left(\frac{q}{\dot{\epsilon}} - \frac{q}{C_3 \cdot h} - f \right) \cdot r + (q - f) \cdot \frac{r \cdot \ln r}{\dot{\epsilon}} \right] \cdot h, \tag{27}$$

$$\frac{\partial \sigma_y}{\partial \dot{\epsilon}} = K \cdot \frac{m}{\dot{\epsilon}} \cdot \left[q \cdot \left(\frac{\epsilon}{C_3 \cdot h} - 1 + \epsilon \right) - f \cdot \epsilon \right] \cdot r \cdot h + \frac{m}{\dot{\epsilon}} \cdot \sigma_y, \tag{28}$$

and

$$\frac{\partial \sigma_y}{\partial T} = K \cdot \frac{-a}{T^2} \cdot \left[q \cdot \left(\frac{\varepsilon}{C_3 \cdot h} - 1 + \varepsilon \right) - f \cdot \varepsilon \right] \cdot r \cdot h + \frac{-a}{T^2} \cdot \sigma_y, \tag{29}$$

where $\frac{\partial f}{\partial \varepsilon}$ in Equation (21) is

$$\frac{\partial f}{\partial \varepsilon} = \left[-C_1 \cdot e^{-C_1 \cdot \varepsilon} + C_2 \cdot \varepsilon^{C_2-1} \right] \cdot \left[1 - e^{-\alpha \cdot \varepsilon} \right] + \left[e^{-C_1 \cdot \varepsilon} + \varepsilon^{C_2} \right] \cdot \alpha \cdot e^{-\alpha \cdot \varepsilon}. \tag{30}$$

For the generalized and modified DSGZ models, terms with the hydrostatic coefficient γ and C_0 should be addressed, as discussed in Section 2.2. It is worth noting that the equations and functions of all DSGZ models are applicable to the 2-D plane strain and 3-D stress; however, they are not yet suitable for 2-D plane stress problems.

2.4. Other Material Models

As mentioned earlier, the computational domain under investigation in the current study encompasses a diversity of materials. Therefore, brief descriptions of the constitutive models used to describe the stress–strain behaviors of these materials other than those described by the DSGZ models, as well as the model parameter identification schemes, are introduced next.

The Johnson–Cook elastoplastic constitutive law [43] stands out as the most extensively employed flow model for simulating high-strain-rate deformation processes in metals, incorporating considerations for plastic strain, plastic strain rate, and temperature. Due to substantial efforts in determining the constitutive flow law parameters for various materials, implementation has been found in numerous finite element codes, including Abaqus. The general expression for the equivalent stress $\bar{\sigma}_y(\bar{\varepsilon}^p, \dot{\bar{\varepsilon}}^p, T)$ is defined by

$$\bar{\sigma}_y(\bar{\varepsilon}^p, \dot{\bar{\varepsilon}}^p, T) = (A + B \cdot \bar{\varepsilon}^p)^n \cdot \left[1 + C \cdot \ln \left(\frac{\dot{\bar{\varepsilon}}^p}{\dot{\bar{\varepsilon}}_0} \right) \right] \cdot \left[1 - \left(\frac{T - T_0}{T_m - T} \right)^m \right], \tag{31}$$

where $\dot{\bar{\varepsilon}}_0$ is the reference strain rate, T_0 is the reference temperature, and T_m is the melting point of material; $A, B, C, n,$ and m are the five constitutive law parameters.

In high- or ultra-high-strain-rate scenarios related to impact dynamics, the impact-induced pressure and temperature usually deviate significantly from those observed in quasi-static deformation situations. Considering the wave front in solids as uniaxial strain compression, the substantial density change alters the volumetric behavior of the material, leading to inaccurate predictions of the stress values when applying the Johnson–Cook model or other hardening flow laws. Therefore, EOS must be introduced to rectify the relationship between volume, pressure, and internal energy. For metals, the Mie–Grüneisen EOS [49,50] exhibits robust performance, as validated by numerous research papers, including our previous study [51]. It establishes a relationship between the pressure and volume of a solid at a specific temperature, thereby determining the instantaneous pressure of an impact-compressed solid. One of the Mie–Grüneisen EOS has a form of

$$p = \frac{\rho_0 \cdot c_0^2 \cdot \left(1 - \frac{\rho}{\rho_0} \right) \cdot \left[1 - \frac{\Gamma_0}{2} \cdot \left(1 - \frac{\rho}{\rho_0} \right) \right]}{\left[1 - s \cdot \left(1 - \frac{\rho}{\rho_0} \right) \right]^2} + \Gamma_0 \cdot \rho_0 \cdot E_m, \tag{32}$$

where the material parameters ρ_0 is the initial density, c_0 is the bulk speed of sound, Γ_0 is the Grüneisen’s gamma at the reference state, $s = \frac{dU_s}{dU_p}$ is a linear Hugoniot slope coefficient derived from the stress wave velocity versus the particle velocity relationship $U_s = c_0 + s \cdot U_p$, and E is the internal energy; for the two variables, p is the pressure, and ρ is the current density.

In the field of solid mechanics, the Johnson–Holmquist II (JH-2) model [52] is used for simulating the mechanical responses of brittle materials, including ceramics, rocks, and

concrete, across varying strain rates. These materials typically possess high compressive strengths but demonstrate relatively low tensile strengths, often manifesting progressive structural damage due to the propagation of microfractures under load. The model reproduces the increase in strength under hydrostatic pressure shown by intact ceramics and the corresponding reduction in strength shown by damaged ceramics. This is achieved by grounding the model on two distinct sets of experimental curves plotting yield stress against pressure, i.e., for intact and damaged materials. Different states are characterized by their respective strengths, presenting the relationship between normalized equivalent stress and normalized pressure. The normalized equivalent stress is expressed as

$$\sigma^* = \sigma_i^* - D \cdot (\sigma_i^* - \sigma_f^*) = \frac{\sigma}{\sigma_{HEL}}, \tag{33}$$

where σ_i^* is the normalized intact equivalent stress, σ_f^* is the normalized fracture stress, D is the damage factor, and σ_{HEL} is the equivalent stress at the Hugoniot elastic limit (HEL is an essential concept representing the net compressive stress at which a 1-D stress wave with uniaxial strain surpasses the elastic limit of the material) [53]. The normalized intact strength and the normalized fracture strength are given by

$$\sigma_i^* = A \cdot (P^* + T^*)^N \cdot (1 + C \cdot \ln \dot{\epsilon}^*) \tag{34}$$

and

$$\sigma_f^* = B \cdot (P^*)^M \cdot (1 + C \cdot \ln \dot{\epsilon}^*) \leq \sigma_{fmax}, \tag{35}$$

where $A, B, C, N,$ and M are material parameters; $P^* = \frac{P}{P_{HEL}}$ is the normalized pressure, in which P and P_{HEL} are the hydrostatic pressure at the instantaneous state and at the HEL; $T^* = \frac{T}{P_{HEL}}$ is the normalized maximum tensile hydrostatic pressure, in which T is the maximum tensile hydrostatic pressure the material can withstand; $\dot{\epsilon}^* = \frac{\dot{\epsilon}}{\dot{\epsilon}_0}$ is the dimensionless strain rate, in which $\dot{\epsilon}_0$ (1.0 s^{-1}) is the reference strain rate; and σ_{fmax} is the ultimate value of σ_f^* that offers additional flexibility in defining the fracture strength. The expression of the accumulated damage due to fracture is given by

$$D = \frac{\sum \Delta \epsilon^p}{\epsilon_f^p} = \frac{\sum \Delta \epsilon^p}{D_1 \cdot (P^* + T^*)^{D_2}}, \tag{36}$$

where $\Delta \epsilon^p$ is the plastic strain during a cycle of integration and ϵ_f^p is the plastic strain to fracture with damage factors of D_1 and D_2 . In addition, the JH-2 model uses the polynomial EOS to characterize the relationship between the hydrostatic pressure P and the volumetric strain $\zeta = \rho/\rho_0 - 1$, which consists of elastic and plastic stages. The functions are expressed as

$$P(\zeta) = \begin{cases} K_1 \cdot \zeta + K_2 \cdot \zeta^2 + K_3 \cdot \zeta^3 + \Delta P & D = 0 \\ K_1 \cdot \zeta + K_2 \cdot \zeta^2 + K_3 \cdot \zeta^3 & 0 < D \leq 1, \\ K_1 \cdot \zeta & Tension \end{cases} \tag{37}$$

where K_1 (bulk modulus), K_2 , and K_3 are constants. In this work, we used parameters from the Abaqus manual example [48] for the JH-2 model.

Flexible materials exhibit nonlinear stress–strain features under relatively large deformations. Under such conditions, they are commonly considered nearly incompressible. Modeling these hyperelastic materials requires the adoption of a constitutive law based on total strain energy density [54,55]. Among various approaches, the Mooney–Rivlin theory [56] is employed, relying on the polynomial Taylor series expansion of the total strain energy. The Mooney–Rivlin constitutive law has previously demonstrated success in accurately predicting the behavior of hyperelastic materials at high strain rates [57,58].

The form of the strain-energy potential W for a two-parameter Mooney–Rivlin model is given by

$$W = C_{10}(\bar{I}_1 - 3) + C_{01}(\bar{I}_2 - 3) + \frac{1}{D_1}(J_{el} - 1)^2, \tag{38}$$

where C_{10} , C_{01} , and D_i are the Mooney–Rivlin parameters, and \bar{I}_1 , \bar{I}_2 , and J_{el} are the first strain invariant, the second strain invariant, and the elastic volumetric strain, respectively. These parameters can be determined by experiments [58].

2.5. Impact Dynamics

Analytically, when a plate (impactor, denoted as 1) hits another plate (target, denoted as 2) at high velocity, compressive stress waves initiate on the impact surface and propagate through each plate. Subsequently, these waves reflect as tensile waves from the free surface of the plates. When the reflected tensile wave propagates through the interface, it separates into a reflective wave and a transmitted wave, particularly if the impactor and target consist of dissimilar materials. This phenomenon resembles the reflection of waves from a free surface, treating air as an insubstantial material with negligible density and longitudinal modulus properties. These concepts are further elaborated in the book [59], which provides insights into longitudinal impact-induced reflection and transmission at a boundary.

Briefly, when impact initiates, the impact-induced velocity and stress in the target are in the form of

$$\left| \vec{v}_2 \right| = \frac{M_1 \cdot c_2}{M_1 \cdot c_2 + M_2 \cdot c_1} \cdot \left| \vec{v}_1 \right| \tag{39}$$

and

$$\sigma_2 = \frac{-M_1 \cdot M_2}{M_1 \cdot c_2 + M_2 \cdot c_1} \cdot \left| \vec{v}_1 \right|, \tag{40}$$

where M is the longitudinal modulus, c is the sound speed of a material, and $\left| \vec{v} \right|$ and σ are the impact velocity and stress along the loading direction. Specifically, $\left| \vec{v}_1 \right|$ represents the initial velocity of the impactor. The longitudinal (P-wave) modulus is defined as the ratio of axial stress to axial strain in a uniaxial strain state, where the neighboring material restricts expansion in the transverse direction. According to Hooke’s law, the longitudinal modulus takes the form of $M = \frac{E \cdot (1-\nu)}{(1+\nu) \cdot (1-2 \cdot \nu)}$. The longitudinal sound speed is therefore

$$c_L = \sqrt{\frac{M}{\rho}} = \sqrt{\frac{E \cdot (1-\nu)}{\rho \cdot (1+\nu) \cdot (1-2 \cdot \nu)}}.$$

Reflection (denoted as r) and transmission (denoted as t) manifest for the incident wave (denoted as i) propagating through discontinuous boundaries, including the interface and free surface. Their velocities and stresses are expressed as

$$\left| \vec{v}_r \right| = \frac{\rho_1 \cdot c_1 - \rho_2 \cdot c_2}{\rho_1 \cdot c_1 + \rho_2 \cdot c_2} \cdot \left| \vec{v}_i \right|, \tag{41}$$

$$\sigma_r = \frac{-\rho_1 \cdot c_1 + \rho_2 \cdot c_2}{\rho_1 \cdot c_1 + \rho_2 \cdot c_2} \cdot \sigma_i = \frac{Z_2 / Z_1 - 1}{Z_2 / Z_1 + 1} \cdot \sigma_i, \tag{42}$$

$$\left| \vec{v}_t \right| = \frac{2 \cdot \rho_1 \cdot c_1}{\rho_1 \cdot c_1 + \rho_2 \cdot c_2} \cdot \left| \vec{v}_i \right|, \tag{43}$$

and

$$\sigma_r = \frac{2 \cdot \rho_2 \cdot c_2}{\rho_1 \cdot c_1 + \rho_2 \cdot c_2} \cdot \sigma_i = \frac{2 \cdot Z_2 / Z_1}{Z_2 / Z_1 + 1} \cdot \sigma_i, \tag{44}$$

where Z is the impact impedance. Adopted from the electric circuit theory, impact impedance is often used to describe problems involving boundaries. This term expresses the ratio of a driving force to the resulting velocity at a given point in the structure and can be converted to $Z = \rho \cdot c$.

3. Modeling and Simulation

We employed Abaqus/Explicit to conduct finite element modeling and simulation of the dynamic impact responses of both a layered composite armor and its constituent materials. A range of constitutive laws and EOS were considered in the simulation of multi-material composites under impact loading. Extensive validation and applications in diverse studies have established the robustness of built-in models from Abaqus in characterizing the stress–strain behavior of simulated materials. For those laws that are not officially supported in Abaqus/Explicit, the VUMAT subroutine provides researchers with a convenient way to test their custom formulations. While prior studies [31] implemented the DSGZ law through VUMAT in Abaqus, its effectiveness was evaluated in this work using the safe-version Newton–Raphson method introduced herein. First, single-element compression tests were conducted to validate the developed DSGZ models through VUMAT. A cube with a 10 mm edge length was modeled and discretized with a single, eight-node linear brick element featuring reduced integration (commonly denoted as C3D8R). Displacement was applied to induce compressive loading on one face, while the opposite face was constrained in the direction of the displacement. Temperature was specified as an input (boundary condition) through predefined fields (298 K). In this work, the parameters of the DSGZ models for all tested polymeric materials were sourced from previously published works [23,46,47,60,61], which are listed in Table 1. Notably, PC_1 and PMMA_1 denote the parameters of PC and PMMA using the generalized DSGZ model, while PC_2 and PMMA_2 represent them using the modified DSGZ model.

Table 1. Material parameters of the generalized and modified DSGZ models for polymers.

| | K (MPa·s ^m) | γ | C_1 | C_2 | C_3 (s ^m) | C_4 | a (K) | α | m |
|---------------------|------------------------------|----------|--------|-------|-------------------------|-------|---------|----------|--------|
| PC_1 ^a | 28.4 | 0.0 | 0.49 | 4.02 | 0.03 | 5.8 | 415 | 6.8 | 0.038 |
| PMMA_1 ^b | 3.9 | 0.0 | 1.91 | 1.49 | 0.0029 | 11.0 | 1191 | 11.7 | 0.064 |
| PA-12 ^c | 3.083 | 0.0 | 0.415 | 2.687 | 3.0 | 200.0 | 870 | 6.6 | 0.01 |
| ABS ^d | 17.85 | 0.4 | 1.83 | 0.2 | 0.06 | 5 | 306 | 50 | 0.044 |
| PBT ^e | 24.5 | 0.0 | 0.32 | 0.12 | 0.1 | 6 | 140 | 200 | 0.058 |
| PC/ABS | 19.85 | 0.0 | −1.324 | 1.984 | 0.021 | 3.58 | 232 | 22.26 | 0.0854 |
| | K (MPa·s ^m) | C_0 | C_1 | C_2 | C_3 (s ^m) | C_4 | a (K) | α | m |
| PC_2 ^f | 8.97 | 1.127 | −0.161 | 1.35 | 0.007 | 100 | 465 | 65 | 0.093 |
| PMMA_2 ^g | 2.7 | 1.582 | −0.76 | 2.443 | 0.03 | 20 | 800 | 18 | 0.138 |

^a Polycarbonate (generalized DSGZ); ^b polymethylmethacrylate (generalized DSGZ); ^c Nylon 12; ^d acrylonitrile butadiene styrene; ^e polybutylene terephthalate; ^f polycarbonate (modified DSGZ); ^g polymethylmethacrylate (modified DSGZ).

After completing the validation of the DSGZ models, we proceeded to construct substantially simpler geometric models characterized by elongated chain shapes. These models were formed using multiple slender straight stripes that depict the column of single representative elements running perpendicular to the surface of the layer. The conceptual framework of such a model bears resemblance to the notion of the representative volume element (RVE) and stands as a reasonable representation of the entire layered armor system. In the simulation of plate impact, the focus is exclusively on the generation and propagation of planar waves along the impact direction. Thus, the model used in this work consists of a “column of single elements” running in the direction normal to the outer surface. While it is possible to model plane wave simulations in a simplified manner, such as a 1-D or 2-D problem with reduced modulus, opting for 3-D elements proves to be more convenient. This approach eliminates the need for conversion of yield equations to accommodate 1-D or 2-D situations, especially for 2-D plane-stress. The “column” displayed in Figure 2 is composed of the impactor, impact-mitigation armor assembly, and protected target. Starting from the impactor positioned adjacent to the outer surface of the armor and moving inward, segments in the representative columns are structured in the sequence of the impactor, front layer, CPM composite layers, base layer, optional backplate, and protected target.

The representative column has a square cross-section with 0.4 mm of equal length for computational efficiency. Segment thicknesses are selected to closely align with typical armor protection applications, such as anti-bullet armor and anti-impact helmets. Given the focus on plane wave propagation in this study, employing complex meshing techniques or varying mesh sizes across segments was unnecessary. All segments were meshed with identical cubic C3D8R elements of 0.2 mm size except for the front layer, anti-crack layer, base layer, and backplate with a small thickness, where the reduced 0.1 mm mesh size was applied. These mesh sizes were determined to be a suitable compromise between accuracy and computational efficiency. Regarding the interactions between each layer, since the primary objective of this work was to investigate the dynamic responses of the composite layers during the initial impact-induced compression stage, these layers were assumed to be perfectly bonded. In this scenario, the “tie” constraint option in the Abaqus interaction definition was employed to simulate the fully bonded condition. The boundary conditions were set to roll on all lateral surfaces of every segment and on the end surface of the protected target.

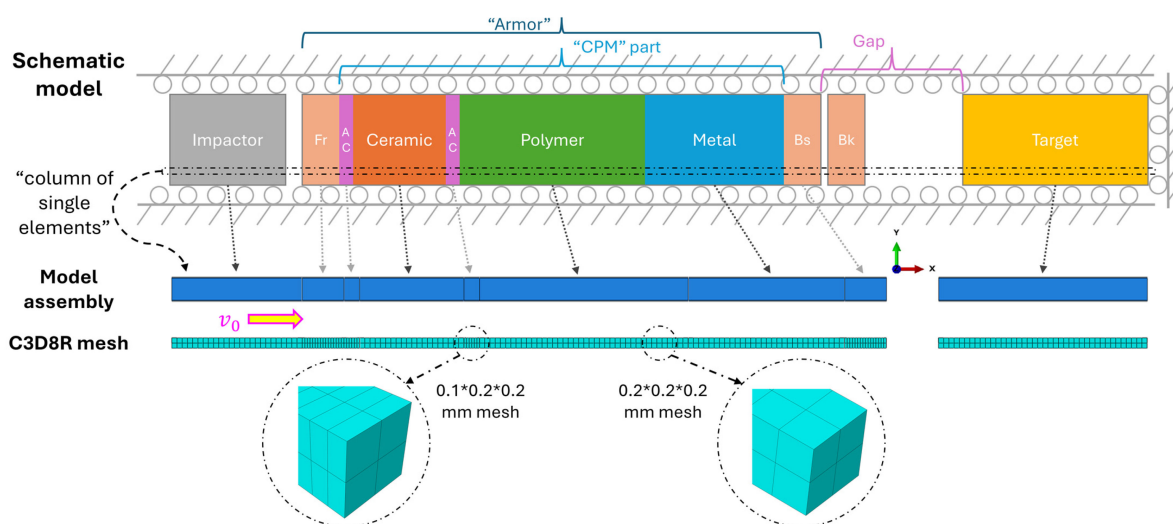


Figure 2. Schematic model and its Abaqus instance of the plate impact simulation.

Before simulating the full armor assembly, we performed individual layer impact simulations using their respective material models. This investigation aimed to analyze fundamental dynamic responses, specifically focusing on velocity and stress at the free surface of the impacted object. These two responses, commonly monitored in experiments using VISAR and manganin gauges, are captured by Equations (39)–(44) and reflect the combined physical and mechanical behaviors under impact loading. In contrast to experimental setups, simulations typically omit the utilization of a backplate to support strain gauges in stress measurement. Given the theoretical assumption that free surface stress is zero, the stress value in this simulation work was consequently recorded at the designated mid-plane of the target. Single-layer tests employed an impactor and target with thicknesses of 20 mm and 10 mm, respectively. Impactor speeds were set at 50 and 100 m s⁻¹. Oxygen-free high thermal conductivity copper (OFHC-Cu) was chosen for the impactor due to its low sound speed and minimal damage during impact compressive loading, facilitating the measurement of dynamic responses (i.e., the steady flat-top of the curves). Therefore, the corresponding initial kinetic energies of the impactor were 35.84 and 143.36 mJ, respectively. This study aimed to explore the effect of the polymer layer on the dynamic responses of the impact-absorbing composites through numerical simulations. We focused on optimizing an armor design with respect to both high strength and high energy absorption by analyzing the influence of layer sequence on the overall structural response. A fixed configuration was established for the front layer, base layer, and optional backplate, comprising 1.6 mm of Steel-4340 constituent. The core CPM composite layer featured three components: a silicon

carbide (SiC) ceramic layer (4.0 mm), a polymer layer (8.0 mm), and an Al-6061 metal layer (6.0 mm). In the design of impact-mitigation armor, ceramic and metal components are commonly used as outer and inner layers in CPM composite. The ceramic layer is intended to absorb the initial impact energy by fracturing, which disrupts the shape and trajectory of the projectile. The metal layer is intended to prevent any fragments that have penetrated the ceramic and polymer layers from reaching the protected target and to provide structural integrity to the composite. Additionally, the polymer layer acts as an impact absorber, which is designed to deform under the impact, absorbing and dispersing the energy of the stress wave. To achieve the goal of this study, we simulated and compared all six possible CPM layer sequences (i.e., C-P-M, C-M-P, P-C-M, P-M-C, M-P-C, and M-C-P). To be consistent with actual armor applications, a crack-proof polyurethane elastomer layer was added as an anti-crack coating (0.6 mm) on both sides of the ceramic layer. To evaluate the performance of the layered composite structure under impact, a protected target (8.0 mm) representing human bone (an ideal model [62] described by the Mie–Grüneisen EOS with shear modulus) was placed in front of it. The protection performance of the CPM composites was directly measured through the responses in the target without a gap to the armor, while an ideal model with a series of gaps of 1.0, 2.0, and 3.0 mm was used for indirect measurements. The former represented the responses from the initial impact stress wave, and the latter served as an idealized depiction of the intricate wave interactions occurring within the armor before hitting the target. The OFHC-Cu impactor size for the composite impact test was set to 5.0 mm, roughly imitating the debris size. The optional backplate was intended to be used to take the same measurements as those in the front layer under the impact. The material properties of the segments, except the DSGZ models, are detailed in Tables 2–5. The speed of the impactor was set to 100 m s^{-1} , resulting in a kinetic energy of 35.84 mJ.

Table 2. Material parameters of the Johnson–Cook model with the Mie–Grüneisen EOS for metals.

| | $\rho \text{ (kg}\cdot\text{m}^{-3}\text{)}$ | $G \text{ (GPa)}$ | $A \text{ (MPa)}$ | B | n | C |
|------------|--|--|-------------------|--|------|------------|
| OFHC-Cu | 8960 | 44.7 | 90 | 292 | 0.31 | 0.025 |
| Steel-4340 | 7830 | 25.9 | 792 | 510 | 0.26 | 0.014 |
| Al-6061 | 2700 | 77.5 | 290 | 204 | 0.35 | 0.011 |
| | m | $\dot{\epsilon}_0 \text{ (s}^{-1}\text{)}$ | $T_m \text{ (K)}$ | $c_0 \text{ (m}\cdot\text{s}^{-1}\text{)}$ | s | Γ_0 |
| | 1.09 | 1.0 | 1356 | 3933 | 1.49 | 1.0 |
| | 1.03 | 1.0 | 1793 | 5350 | 1.34 | 2.0 |
| | 1.34 | 1.0 | 858 | 4578 | 1.33 | 1.67 |

Table 3. Material parameters of the JH–2 model for the ceramic.

| | $\rho_0 \text{ (kg}\cdot\text{m}^{-3}\text{)}$ | $G \text{ (GPa)}$ | A | N | B | M |
|-----|--|--|---------------------|--------------------------------|--------------------------------|-------------------------------|
| SiC | 3251 | 193 | 0.96 | 0.65 | 0.35 | 1.0 |
| | C | $\dot{\epsilon}_0 \text{ (s}^{-1}\text{)}$ | $T \text{ (GPa)}$ | $\sigma_i^{max} \text{ (GPa)}$ | $\sigma_f^{max} \text{ (GPa)}$ | HEL (GPa) |
| | 0.009 | 1.0 | 0.75 | 12.2 | 1.3 | 11.7 |
| | $p_{HEL} \text{ (GPa)}$ | β | D_1 | D_2 | $\bar{\epsilon}_{f,max}^{pl}$ | $\bar{\epsilon}_{f,min}^{pl}$ |
| | 5.13 | 1.0 | 0.48 | 0.48 | 1.2 | 0.0 |
| | FS | IDamage | $K_1 \text{ (GPa)}$ | $K_2 \text{ (GPa)}$ | $K_3 \text{ (GPa)}$ | |
| | 0.2 | 0 | 220 | 361 | 0 | |

Table 4. Material parameters of the Mooney–Rivlin model for polyurethane (PU) elastomer.

| | C_{10} | C_{01} | D_1 |
|--------------|----------|----------|----------|
| PU elastomer | 77.69 | −37.66 | 0.000251 |

Table 5. Material parameters of the elastic EOS model for the human bone.

| | G (GPa) | c_0 (m·s ⁻¹) | s | Γ_0 |
|------|---------|----------------------------|------|------------|
| Bone | 2.664 | 1850 | 0.94 | 0.0 |

4. Results and Discussion

Within the scope of the present work and the limitations of the constitutive models used, we aimed to explore the dynamic responses of the material systems subjected only to the compressive wave without considering the potential dynamic tensile failure, e.g., the spall fracture due to the superposition of two tensile waves. For the polymers, we present the results for the VUMAT subroutine validation on the DSGZ models via a single cubic element in Section 4.1. After confirming the effectiveness of the VUMAT subroutine, the results for subsequent single-layer and multi-layer composite impact tests in investigating the dynamic responses and the layer sequence effects were discussed in Sections 4.2–4.4, respectively.

4.1. VUMAT Subroutine Validation

To evaluate the effectiveness of the VUMAT subroutine developed in the present work, several polymer materials from both the original DSGZ paper [23,46,60] and recent publications [47] were selected (Table 1) to reproduce their stress–strain curves via single cubic element compression tests. As shown in Figure 3, the generalized DSGZ model successfully predicts the stress–strain curves for PC_1, PMMA_1, and PA-12 across a broad strain rate range (10⁻³ to 10² s⁻¹). However, its performance deteriorates notably for ABS and PBT at a high strain rate (10³ s⁻¹). Further evaluation with a pre-calibrated DSGZ parameter set for PC/ABS at 1600 and 5000 s⁻¹ reveals satisfactory agreement with the experimental data at 1600 s⁻¹, but significant deviation is observed within the initial elastic region at 5000 s⁻¹. These results suggest that the generalized DSGZ model, essentially equivalent to the standard DSGZ model in this context, often struggles to accurately predict high-strain-rate responses for various polymers due to its inherent limitations in describing the initial elastic and yield stress shift behavior. Subsequently, high-strain-rate tests were conducted on PC_2 and PMMA_2, employing material properties calibrated from the corresponding modified DSGZ model. The obtained results exhibit good agreement with the experimental data for these two materials, demonstrating their suitability for incorporation into our CPM composite impact simulations. In brief, the effectiveness of our VUAMT implementation for the DSGZ models in Abaqus/Explicit has been validated to be applicable in simulating the mechanical behavior of polymers.

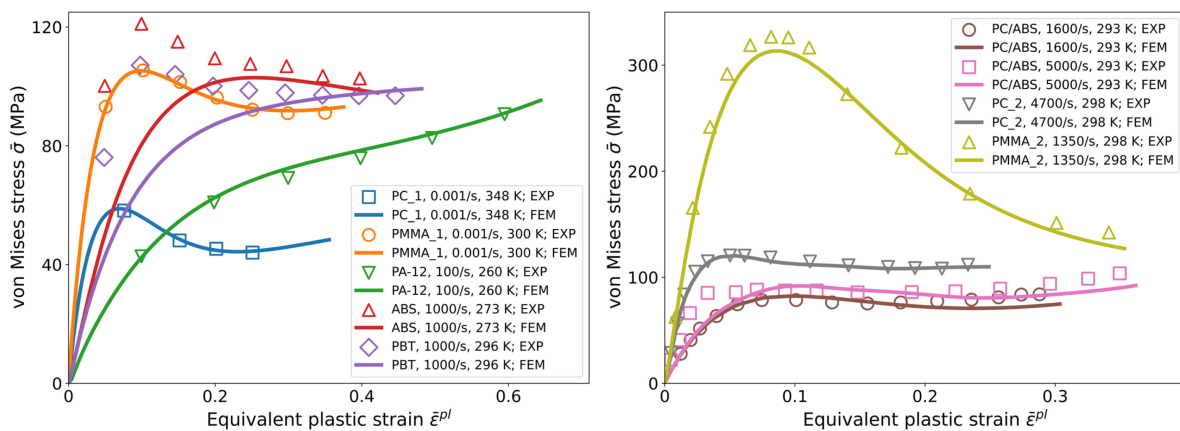


Figure 3. VUMAT subroutine validation for the generalized and modified DSGZ models with material parameters sourced from previous studies [23,46,47,60,61].

4.2. Dynamic Responses of the Single-Layer Target

Our previous investigation [51] successfully employed the plate impact simulation method to study the dynamic response of metals under high-strain-rate loading using the Johnson–Cook model with the Mie–Grüneisen EOS. Due to their exceptional resistance to ultra-high-strain-rate impacts, metals excel in extreme impact-mitigation applications, effectively handling velocities exceeding thousands of meters per second. Organic polymeric materials, while exhibiting lower elastic moduli than metals, can undergo significant deformations but have limited tolerance for ultra-high strain rates (typically below 10^5 s^{-1}). To comply with the available parameters of the DSGZ constitutive law at high strain rates, we first performed single-layer impact tests with impact velocities from 5 to 50 m s^{-1} to determine the actual strain rates in the polymer targets. Therefore, the volumetric strain rate was subsequently obtained from an element located in the mid-plane of the simulated target. Upon wave passage, the element began to deform, reaching a steady state (a compressed state with constant strain) after the wave front went away. As Figure 4a illustrates, only the 5 m s^{-1} PC/ABS case exhibited a strain rate on the order of 10^3 , while the other two cases readily attained rates exceeding 10^4 . This seems to surpass the predictive capability of the DSGZ model with parameters calibrated at 5000 s^{-1} for PC/ABS [63]. Despite a higher compressive element strain rate of $65,000 \text{ s}^{-1}$ observed in the 50 m s^{-1} PC/ABS case, the relatively low volumetric strain (0.03) and equivalent plastic strain rate (0.012 in Figure 4c) cause a low von Mises stress at steady compressive state (25 MPa in Figure 4d), which is significantly below the yield strength. Compared to the large deformation DSGZ validation curve (Figure 4b), this 0.012 equivalent plastic strain value signifies the early stage of plastic deformation, far from yield or softening. Similar trends and values were observed in the responses of PA-12, PC_2, and PMMA_2 at the mentioned velocities. This behavior can be attributed to the dynamic nature of plate impact compared to conventional quasi-static or continuous high-speed loadings. In plate impact, unless the impactor possesses significantly greater mass and volume than the target, the initial velocity of the impactor rapidly decays as stress waves propagate in both the impactor and the target. Due to this non-continuous velocity and the inherent characteristics of plate impact, the element (treated as an RVE) remains in a steady compressive state until the release wave arrives. Consequently, the impact loading with a pulse-like, high volumetric strain rate during impact typically does not induce significant deformation unless the impactor carries higher kinetic energy. Furthermore, the stress–strain curves from previous studies [47], which were utilized for the DSGZ parameter calibration at high strain rates, also exhibit similar initial elastic values (less than 0.05 strain). Therefore, the parameters calibrated at 10^3 s^{-1} strain rate can be confidently applied to higher strain rate problems, such as the plate impact simulation in this work.

Due to the limitations of our impact tube facility, the impactor velocity was restricted to 100 m s^{-1} in the simulations, providing relevant guidance for the ongoing experiments. In single-layer tests, a further reduction to 50 m s^{-1} was implemented to prevent some uncertainties due to the lack of availability of DSGZ parameters for ultra-high strain rates. Several materials, including PC/ABS, PC_2, and PMMA_2, were chosen for the test due to their availability of DSGZ parameters at relatively high strain rates. Free surface velocity and mid-plane stress were recorded for these polymers alongside the metal and ceramic reference materials, as shown in Figure 5. Notably, both the polymer and non-polymer layers exhibit a sharp initial rise, followed by steady, top-flat curves, indicating the robustness of our VUMAT subroutine implementation of DSGZ for polymers compared to native Abaqus models for metals and ceramics. These steady, free surface velocity and mid-plane stress values (impact direction along the x -axis) are consistent with the theoretical calculations using Equations (39)–(44). Interestingly, at 50 m s^{-1} , the polymers exhibit higher free surface velocities, but significantly lower stresses compared to non-polymeric materials, highlighting their distinct, dynamic material behavior. Furthermore, Figure 5 reveals promising noise reduction with the general contact method, as demonstrated by

the rapid decay of noise into straight lines, mitigating concerns about numerical errors in these plate impact simulations.

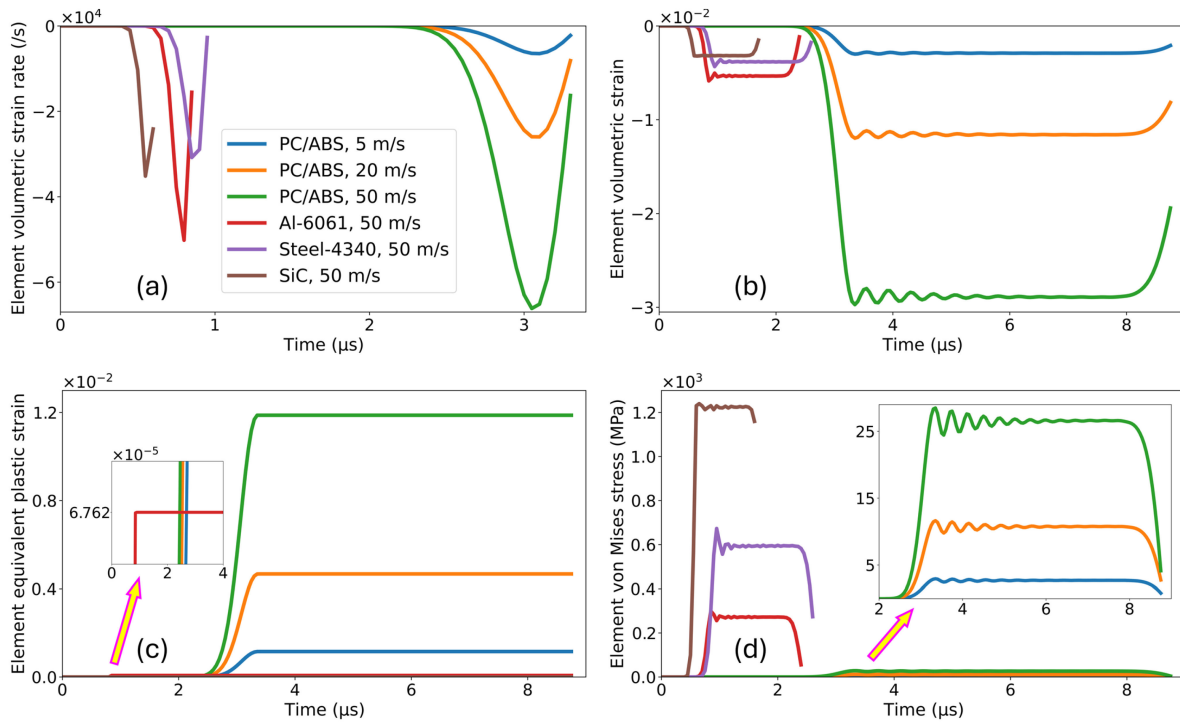


Figure 4. Dynamic responses of PC/ABS, Al-6061, Steel-4340, and SiC as a single layer in terms of (a) volumetric strain rate, (b) volumetric strain, (c) equivalent plastic strain, and (d) von Mises stress during the impact compressive wave passing through an element in the mid-plane of the target.

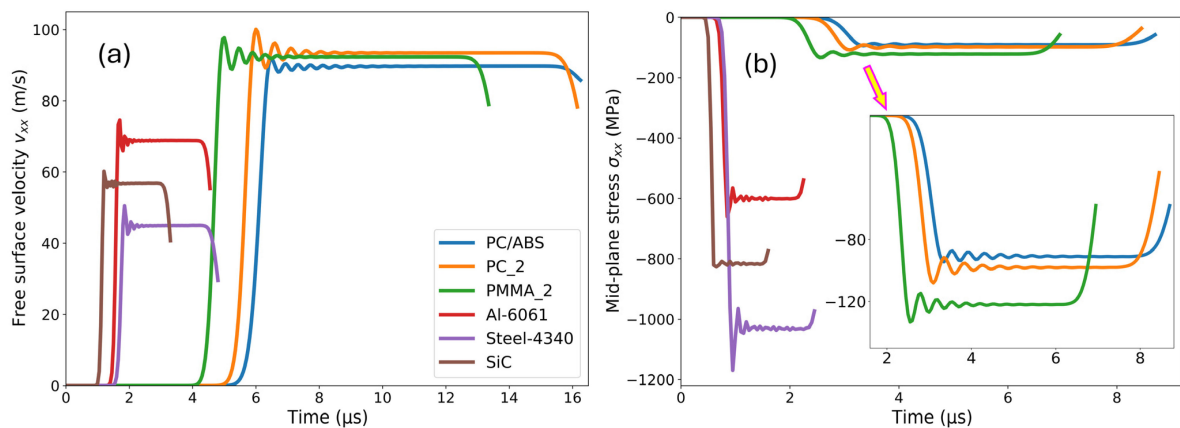


Figure 5. Dynamic responses of PC/ABS, PC₂, PMMA₂, Al-6061, Steel-4340, and SiC as a single layer represented by (a) free surface velocity and (b) mid-plane stress during the 50 m s⁻¹ impact.

4.3. Dynamic Responses of the CPM Composite

A multi-layer, impact-mitigation armor typically consists of distinct functional layers, such as strength-bearing, energy-absorbing, support, and anti-crack layers. While advanced composites often integrate some of these functionalities into a single layer, in this study, for simplicity, we utilize pure polymers and non-polymeric materials in simulated plate impact experiments. Considering the relative softness of PC compared to PMMA, with the latter resembling light metals like aluminum, PC was chosen as the polymer layer in the composite assembly. To accurately predict the mechanical behavior of the polymer layer, the modified DSGZ model was employed with PC₂ material properties in the assembly, allowing us to investigate the influence of layer sequence on the impact-mitigation

performance. As depicted in Figure 2, all segments maintain fixed thickness and position except for the switchable layer sequence in the composite part. This consistency enables the measurement and comparison of dynamic responses at identical time periods, including the crucial free surface velocity, internal stress, and strain energy during wave propagation.

The effectiveness of halting objects, particularly debris, stands as a pivotal determinant in evaluating the overall performance of armor. Figure 6a illustrates a significant occurrence in the interface velocity (equivalent to the free surface velocity), which abruptly drops to 45 m s^{-1} from its initial value of 100 m s^{-1} . Subsequently, it rises to 80, 90, and 65 m s^{-1} when the first composite layer comprises ceramic, polymer, and metal, respectively. Owing to the disparate impact impedance of these layers, the arrival timing of each reflected wave at this specific interface point exhibits dissimilarities, leading to observable variations in the velocity trends. Despite the intricacies involved in analyzing the complex propagation of stress waves to precisely elucidate the mechanism behind such distinct velocity responses for different first composite layers, it is evident that a metal as the outer layer (referred to as the “first layer” later) offers optimal impactor stopping capability, while a polymer performs inadequately. Upon the arrival of the compressive stress wave, the free surface of the backplate manifests a brief kinetic response period, thereby providing insight into the overall performance of the armor system during the initial intense impact. Figure 6b reveals that C-P-M and P-C-M configurations exhibit lower velocity responses compared to C-M-P and M-C-P. This aligns with the observations in Figure 6a, highlighting the trend of lower velocities with metal layers, regardless of placement in the first or third layer. This can be attributed to the diverse energy absorption capacities of these materials, such as strain energy storage. Although intricate wave propagation may cause further velocity increases (Figure 6b), we did not analyze post-impact responses or material behaviors beyond the initial free surface wave arrival. Numerous publications have extensively covered failures and damages during tensile wave interactions [64–66]. The absence of damage models in this study limits our investigation of possible spall phenomena similar to those explored in our previous work [51].

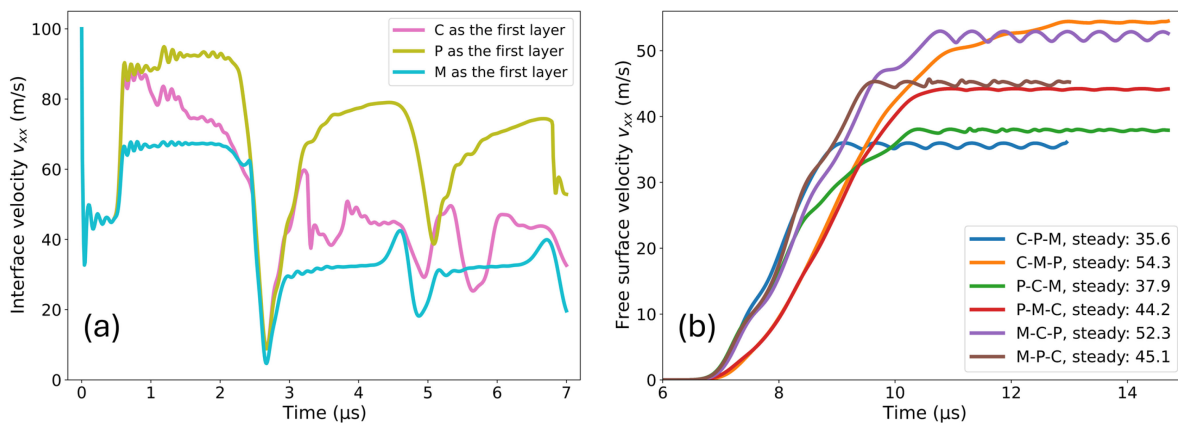


Figure 6. Dynamic responses of (a) the interface velocity of the impactor with different first composite layers and (b) the free surface velocity of the backplate with different layer sequences.

To elucidate the differences in the free surface velocity of the backplate observed in distinct layer sequence configurations, we extended our investigation to include a comparison of strain energy and kinetic energy between the initial impact on the front layer (the impactor hits the front layer) and the subsequent impact on the backplate (the composite assembly hits the backplate). The extraction of the element strain energy and kinetic energy was performed on a mid-plane element of both the front layer and backplate. This comparison is robust due to the identical nature of the front layer and backplate across all configurations. As depicted in Figure 7a, the front layer exhibits a consistent pulse-like strain energy response until the arrival of a reflected wave originating from the

discontinuous interface with the first composite layer. Behind the wave front, the front layer retains substantial strain energy of 11.2 μJ if the metal is the first layer, whereas only 0.7 μJ of strain energy is stored when the first composite layer is a polymer. This implies that potential energy is more readily transferred (dissipated) to the polymer than to the metal. A gradual increase in the strain energy following the initial drop, which is observed for a ceramic first layer, suggests complex wave interactions within the ceramic due to its JH-2 material definition, which allows for plastic sub-wave generation and failure. In contrast, the strain energy of the backplate (all six configurations) is significantly lower (below 0.27 μJ), demonstrating the effectiveness of the CPM composite structure in mitigating the intense impact load. Furthermore, the responses of the element kinetic energy, as depicted in Figure 7b, align with the velocity profile in Figure 6. The utilization of the CPM composite results in a consistent reduction in the kinetic energy by at least 35% (from 70.7 μJ for “M as the 1st layer” to 46.3 μJ for “M-C-P”), further emphasizing the efficacy of the CPM composite in this context.

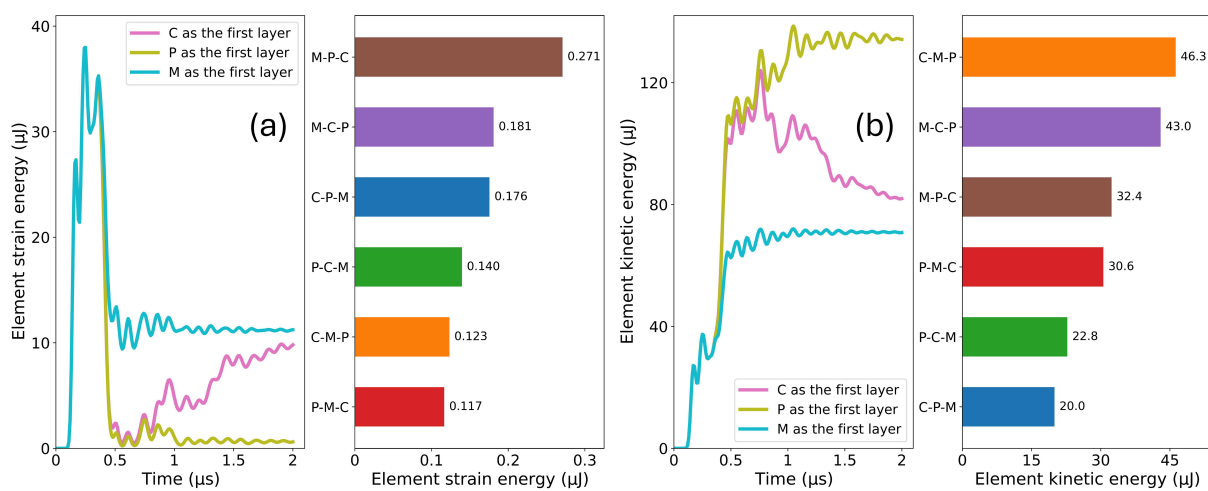


Figure 7. Element energy histories of the front layer with different first composite layers and the backplate with different layer sequences in terms of (a) strain energy and (b) kinetic energy.

4.4. Layer Sequence Effect on the Protected Target

While this study focuses on implementing the DSGZ models in the VUMAT subroutine for the dynamic response of the polymer layer, particularly its impact compression behavior, without considering subsequent tensile failure and damage, we ultimately aim to understand the performance of polymer composites in impact-mitigation applications. Specifically, we were interested in using the simulation results to determine the effect of layer sequence on the energy absorption capability of the composite to guide ongoing impact experiments, which are critical for designing optimal armor systems. Despite our ability to draw some promising observations regarding the effect of layer sequencing, identifying the overall potential energy and kinetic energy in the composite structure proves challenging due to the intrinsic characteristics of explicit dynamic problems, where waves move back and forth within objects. Consequently, we conducted an additional set of simulations involving a protected target (without a backplate at this stage) to equivalently assess the overall energy levels of the entire armor assembly for various sequence configurations. As detailed in Section 3, the chosen protected target emulated human bone, featuring an elastic EOS material. Consistent with our focus, we only considered the compressive wave from the initial impact (armor hits the target) and measured the velocity and stress from the mid-plane of the target. It is important to note that substantial wave interactions occurred within the armor before hitting the target for the gap case (indirect measurement). Nevertheless, due to the absence of a damage model and the relatively mild impact speed of 100 m s^{-1} , which is typically insufficient to induce spallation, this idealized model serves only as a simple demonstration.

The study in Section 4.3 demonstrated the crucial role of a directly attached backplate in analyzing the energy absorption of armor assemblies by eliminating the gap between the armor and the target. Inherently, Figure 8 clearly reveals the dynamic response and mechanical behavior of the target under initial impact stress waves. These mid-plane velocity and stress measurements definitively explain the influence of layer sequence on the overall energy absorption, as intricate wave interactions occur primarily behind the fastest initial compressive wave. Compared to a pure ceramic or metal, the inclusion of polymer in the CPM composites leads to superior impact mitigation, as evidenced by at least 40% lower velocity and stress (57 vs. 98 m s⁻¹ and -203 vs. -344 MPa for M-C-P vs. pure ceramic in circled points indicating the arrival timing of the reflected wave from the end). Notably, composites with metal as the third layer exhibited the most impressive performance, aligning with the low strain and kinetic energy observed in the backplate due to the metallic component (see Figure 7). Removing the compliant polymer from the third layer (neither C-M-P nor M-C-P cases) also enhances the armor performance by at least 100% compared to stiff materials, confirming previous findings on the beneficial role of polymers in bilayer or sandwich structures [14]. However, contrary to a previous study [17], placing the polymer in the third layer (C-M-P and M-C-P cases) unexpectedly resulted in a performance reduction, and their responses were even worse than those of the pure polymer. This discrepancy may be attributed to the additional layers present in our work compared to the bilayer structure studied previously. Overall, for optimal impact mitigation on directly attached targets, the P-C-M or C-P-M configurations are recommended for CPM composites. When using the P-C-M sequence, the polymer layer first absorbs some of the impact energy, reducing the shock transmitted to the ceramic layer. This can help prevent premature fracturing of the ceramic, reducing the peak stress transmitted to the metal layer. On the other hand, in the C-P-M sequence, the hard ceramic layer is the first to encounter the impactor. The impactor is disrupted by altering wave interactions, specifically wave transmission and reflection, while the initial impact energy is absorbed by fracturing. The polymer layer then absorbs and disperses the stress wave, reducing the peak stress transmitted to the metal layer. In these two sequences, the metal layer serves as the inner layer and plays an important role compared to the other two materials, as it stores impact energy through partial plastic deformation while providing structural support. The CPM composite has potential mechanisms for impact mitigation, including energy absorption (by the polymer and metal layers), impactor disruption (by the ceramic layer), and stress dispersion (by the polymer layer). This is why the composite performs better than individual layers.

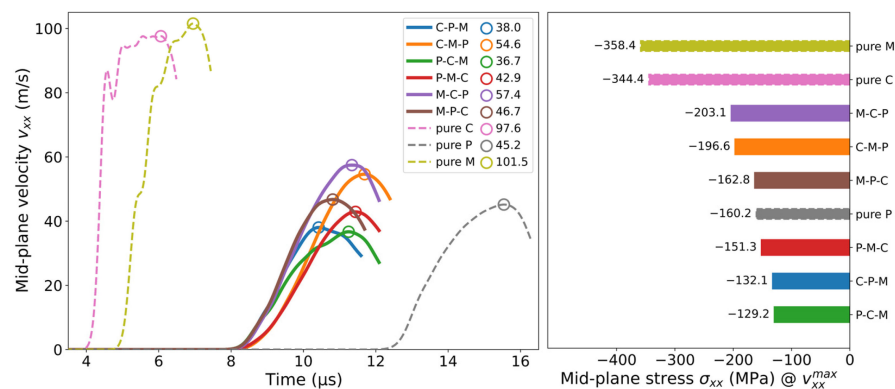


Figure 8. Mid-plane velocity history and corresponding stress at maximum velocity of the protected target for different layer sequences, with no initial gap to the armor; pure ceramic, polymer, and metal layers are plotted as the reference using dashed lines or dashed outlines.

Figure 9 presents the velocity and stress profiles of the armor configurations with the initial gap distances of 1.0, 2.0, and 3.0 mm. Analyzing these profiles reveals no readily discernible trend or rule to draw definitive conclusions about their performance in im-

compact mitigation. This ambiguity arises from the intricate interaction of multiple waves, transmitting through and reflecting from each interface between the layers with disparate impedances, leading to highly time-dependent behavior within the armor assembly, especially the free surface of the component. Therefore, diverse velocity and stress responses in the protected target were generated. Regardless of the gap distances, the C-P-M and M-P-C sequences exhibit the most optimal impact mitigation performance, characterized by relatively low values for both velocity and stress, indicating that the stiff-compliant-stiff structural sequence is more prominent than other sequences in the composite design. Notably, the C-P-M sequence outperforms the M-P-C, suggesting that placing the ceramic as the first layer facing the impact and the metal as the innermost layer for energy absorption further optimizes the overall armor performance. The influence of gap distance on the impact response in the CPM composite exhibits distinct patterns in all cases. At 1.0 mm, the responses are almost within a similar range of value except for the C-M-P case. For larger gap distances of 2.0 and 3.0 mm, the P-M-C and M-C-P cases present exceptional performance, respectively. This suggests a strong dependence of the target response on the actual stress wave distribution within the CPM composite at impact, as observed previously [67]. Details of the stress wave distribution effect on the target response with gaps will be analyzed in our future communications.

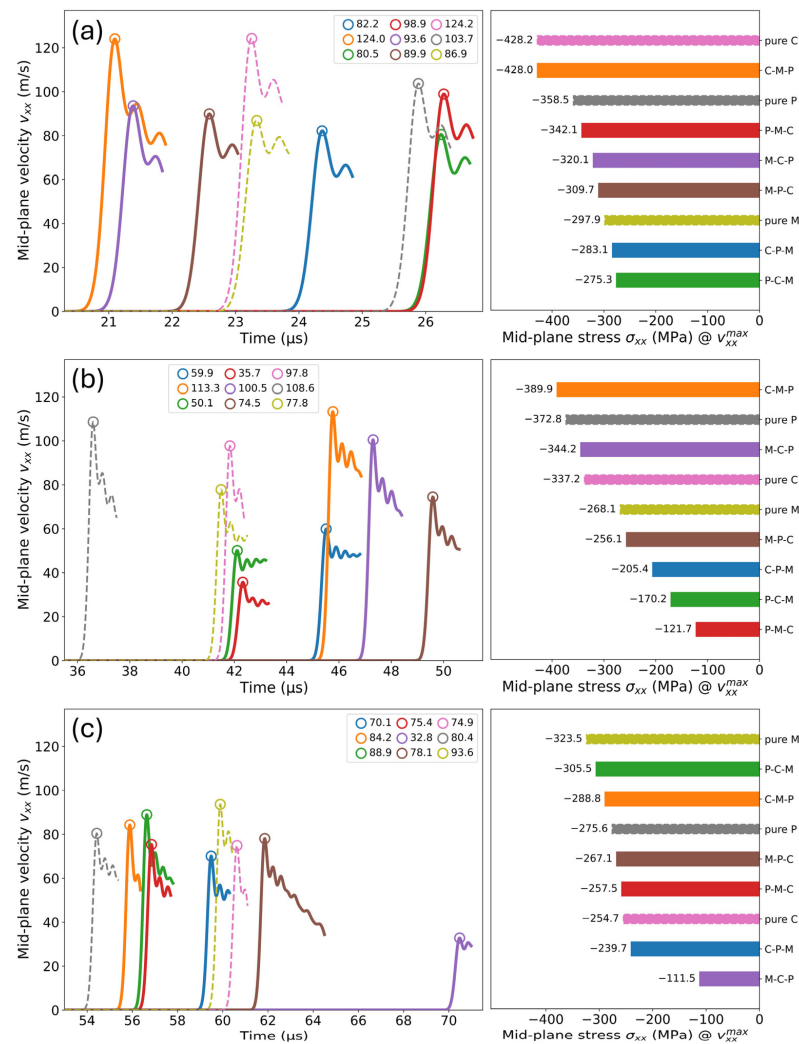


Figure 9. Mid-plane velocity history and corresponding stress at maximum velocity of the protected target for different layer sequences, with the initial gap distances of (a) 1.0, (b) 2.0, and (c) 3.0 mm to the armor; pure ceramic, polymer, and metal layers are plotted as the reference using dashed lines or dashed outlines.

Beyond the simplistic three-layer configurations studied here, practical applications of composite assemblies often necessitate more complex material arrangements. Consequently, the conclusions drawn from the C-P-M and P-C-M stiff-compliant-stiff configurations may not directly translate to real-world scenarios. The enhancement of performance in fundamentally layered polymer composites can be achieved by incorporating more advanced functional layers. Nevertheless, the insights gained from the aforementioned results remain valuable and contribute significantly to the understanding of individual and collective material behavior in a composite assembly. This understanding, in turn, aids in the selection of suitable configurations for experimental tests of layered polymer composite systems.

5. Conclusions

In our simulation study, we explored the dynamic responses of layered ceramic–polymer–metal (CPM) composites under plate impact. Our investigation is based on the successful implementation of the generalized and modified DSGZ phenomenological constitutive laws via VUMAT subroutines in Abaqus/Explicit. The combination of finite element simulations conducted on the Abaqus platform with the DSGZ models for polymers and other constitutive models, such as the JH-2 and Johnson–Cook models for ceramics and metals, demonstrated its effectiveness. This research not only deepens our comprehension of how composite materials respond to impact loads but also aids in the creation of precise material models and the improvement of simulation methods. We observed variations in the impact-induced dynamics of these layered composites, including distinct free surface velocity and mid-plane internal stress during stress wave propagation, which underscore the sensitivity of the composite's response to the arrangement of its constituent layers. Importantly, some layer sequences might demonstrate improved energy absorption capabilities, whereas others could distribute stress more efficiently. Among the composite sequences we investigated, the P-C-M and C-P-M configurations, which have the metal as the innermost layer, exhibited outstanding impact mitigation performance. This finding implies that the strategic arrangement of the polymer layers within the composite structure could considerably enhance the overall energy absorption, highlighting the significance of customizing material configurations to meet specific application needs. The ambiguous outcomes for the protected target, especially when simulated with initial gap distances that closely resemble real-world situations, emphasize the necessity for an in-depth analysis of stress wave interactions to provide accurate descriptions by collecting more simulation cases. Furthermore, the complex wave interactions due to shock impedance mismatch between ceramics, polymers, and metals in the composite structure introduce complicated dynamic responses that require further examination.

In summary, we implemented the DSGZ models in Abaqus/Explicit using VUMAT subroutines to simulate the mechanical behavior and dynamic response of common polymeric materials. We designed a numerical modeling framework to match our plate impact experiments. Through the analysis of impact simulations on single-layer polymer components and three-layer CPM composite materials, we were able to determine the dynamic behavior of polymer components. Additionally, we examined the effect of layer sequence on impact mitigation at varying distances between the armor and the protected target. Although there are limited conclusions regarding the dynamic responses in the protected target due to insufficient case studies, the effect of layer sequence on overall impact mitigation performance can still provide insights to optimize our experiments. It helps in understanding the behavior of different materials with their unique properties on the performance of the composite under impact loads. The ceramic layer helps with impactor dispersion, the polymer and metal layers aid in energy absorption, and the metal layer assists with stress dispersion. By integrating empirical data with simulation methods, predictive models can be developed through parameter study. These models can predict the performance of composites under various impact conditions, aiding in the design of more effective impact mitigation systems.

Author Contributions: Conceptualization, H.Z., S.N., A.A.-O. and S.J.; methodology, H.Z. and A.A.-O.; software, H.Z.; validation, H.Z. and S.J.; investigation, H.Z. and S.J.; writing—original draft, H.Z. and S.J.; writing—review and editing, A.M.R., M.K.S., S.L. and S.N.; supervision, S.J., A.A.-O., S.L. and M.K.S. All authors have read and agreed to the published version of the manuscript.

Funding: This research was supported by the U.S. Army Corp of Engineers, Engineering Research and Development Center (ERDC) (Grant Numbers. W912HZ2020042 and W912HZ21C0040).

Data Availability Statement: The data that support the findings of this study are openly available on GitHub at <https://github.com/hzhangolemiss/VUMAT-DSGZs> (accessed on 12 April 2024).

Acknowledgments: S.J. acknowledges the support provided by the U.S. Army ERDC under Contract W912HZ2020042. S.N. and A.A.-O. acknowledge the support provided by the U.S. Army ERDC under Contract W912HZ21C0040. The use of trade, product, or firm names in this article is for descriptive purposes only and does not imply endorsement by the U.S. Government. The tests described and the resulting data presented herein were obtained from research conducted under the Installations and Operational Environments Program of the United States Army Corps of Engineers—Engineer Research and Development Center. Permission was granted by the Chief of Engineers to publish this information. The findings of this report are not to be construed as an official Department of the Army position unless so designated by other authorized documents.

Conflicts of Interest: The authors declare no conflicts of interest.

References

1. Zhang, X.; Xu, Y.; Zhang, X.; Wu, H.; Shen, J.; Chen, R.; Xiong, Y.; Li, J.; Guo, S. Progress on the Layer-by-Layer Assembly of Multilayered Polymer Composites: Strategy, Structural Control and Applications. *Prog. Polym. Sci.* **2019**, *89*, 76–107. [CrossRef]
2. Stephen, C.; Shivamurthy, B.; Mohan, M.; Mourad, A.-H.I.; Selvam, R.; Thimmappa, B.H.S. Low Velocity Impact Behavior of Fabric Reinforced Polymer Composites—A Review. *Eng. Sci.* **2022**, *18*, 75–97. [CrossRef]
3. Tasdemirci, A.; Hall, I.W.; Gama, B.A.; Guden, M. Stress Wave Propagation Effects in Two- and Three-Layered Composite Materials. *J. Compos. Mater.* **2004**, *38*, 995–1009. [CrossRef]
4. Zhuang, S.; Ravichandran, G.; Grady, D.E. An Experimental Investigation of Shock Wave Propagation in Periodically Layered Composites. *J. Mech. Phys. Solids* **2003**, *51*, 245–265. [CrossRef]
5. Oladele, I.O.; Omotosho, T.F.; Adediran, A.A. Polymer-Based Composites: An Indispensable Material for Present and Future Applications. *Int. J. Polym. Sci.* **2020**, *2020*, 8834518. [CrossRef]
6. Agrawal, S.; Singh, K.K.; Sarkar, P. Impact Damage on Fibre-Reinforced Polymer Matrix Composite—A Review. *J. Compos. Mater.* **2014**, *48*, 317–332. [CrossRef]
7. Park, R.; Jang, J. Impact Behavior of Aramid Fiber/Glass Fiber Hybrid Composites: The Effect of Stacking Sequence. *Polym. Compos.* **2001**, *22*, 80–89. [CrossRef]
8. Lopes, C.S.; Camanho, P.P.; Gürdal, Z.; Maimí, P.; González, E.V. Low-Velocity Impact Damage on Dispersed Stacking Sequence Laminates. Part II: Numerical Simulations. *Compos. Sci. Technol.* **2009**, *69*, 937–947. [CrossRef]
9. Mousavi, M.V.; Khoramshad, H. Investigation of Energy Absorption in Hybridized Fiber-Reinforced Polymer Composites under High-Velocity Impact Loading. *Int. J. Impact Eng.* **2020**, *146*, 103692. [CrossRef]
10. Schwab, M.; Pettermann, H.E. Modelling and Simulation of Damage and Failure in Large Composite Components Subjected to Impact Loads. *Compos. Struct.* **2016**, *158*, 208–216. [CrossRef]
11. Mullaoglu, F.; Usta, F.; Türkmen, H.S.; Kazancı, Z.; Balkan, D.; Akay, E. Deformation Behavior of the Polycarbonate Plates Subjected to Impact Loading. *Procedia Eng.* **2016**, *167*, 143–150. [CrossRef]
12. Zhang, W.; Tekalur, S.A.; Huynh, L. Impact Behavior and Dynamic Failure of PMMA and PC Plates. In *Dynamic Behavior of Materials*; Proulx, T., Ed.; Conference Proceedings of the Society for Experimental Mechanics Series; Springer: New York, NY, USA, 2011; Volume 1, pp. 93–104. ISBN 978-1-4419-8227-8.
13. Antoine, G.O.; Batra, R.C. Low Speed Impact of Laminated Polymethylmethacrylate/Adhesive/Polycarbonate Plates. *Compos. Struct.* **2014**, *116*, 193–210. [CrossRef]
14. Tekalur, S.A.; Shukla, A.; Shivakumar, K. Blast Resistance of Polyurea Based Layered Composite Materials. *Compos. Struct.* **2008**, *84*, 271–281. [CrossRef]
15. McShane, G.J.; Stewart, C.; Aronson, M.T.; Wadley, H.N.G.; Fleck, N.A.; Deshpande, V.S. Dynamic Rupture of Polymer–Metal Bilayer Plates. *Int. J. Solids Struct.* **2008**, *45*, 4407–4426. [CrossRef]
16. Stergiou, T.; Baxevanakis, K.P.; Roy, A.; Sazhenkov, N.A.; Nikhamkin, S.M.; Silberschmidt, V.V. Impact of Polyurea-Coated Metallic Targets: Computational Framework. *Compos. Struct.* **2021**, *267*, 113893. [CrossRef]
17. Amini, M.R.; Simon, J.; Nemat-Nasser, S. Numerical Modeling of Effect of Polyurea on Response of Steel Plates to Impulsive Loads in Direct Pressure-Pulse Experiments. *Mech. Mater.* **2010**, *42*, 615–627. [CrossRef]
18. Chu, D.; Li, Z.; Yao, K.; Wang, Y.; Tian, R.; Zhuang, Z.; Liu, Z. Studying the Strengthening Mechanism and Thickness Effect of Elastomer Coating on the Ballistic-Resistance of the Polyurea-Coated Steel Plate. *Int. J. Impact Eng.* **2022**, *163*, 104181. [CrossRef]

19. Jerabek, M.; Major, Z.; Lang, R.W. Uniaxial Compression Testing of Polymeric Materials. *Polym. Test.* **2010**, *29*, 302–309. [CrossRef]
20. Lin, P.; Cheng, S.; Wang, S.-Q. Strain Hardening During Uniaxial Compression of Polymer Glasses. *ACS Macro Lett.* **2014**, *3*, 784–787. [CrossRef] [PubMed]
21. Richeton, J.; Ahzi, S.; Vecchio, K.S.; Jiang, F.C.; Adharapurapu, R.R. Influence of Temperature and Strain Rate on the Mechanical Behavior of Three Amorphous Polymers: Characterization and Modeling of the Compressive Yield Stress. *Int. J. Solids Struct.* **2006**, *43*, 2318–2335. [CrossRef]
22. G'sell, C.; Jonas, J.J. Determination of the Plastic Behaviour of Solid Polymers at Constant True Strain Rate. *J. Mater. Sci.* **1979**, *14*, 583–591. [CrossRef]
23. Duan, Y.; Saigal, A.; Greif, R.; Zimmerman, M.A. A Uniform Phenomenological Constitutive Model for Glassy and Semicrystalline Polymers. *Polym. Eng. Sci.* **2001**, *41*, 1322–1328. [CrossRef]
24. Wang, J.; Xu, Y.; Zhang, W. Finite Element Simulation of PMMA Aircraft Windshield against Bird Strike by Using a Rate and Temperature Dependent Nonlinear Viscoelastic Constitutive Model. *Compos. Struct.* **2014**, *108*, 21–30. [CrossRef]
25. Zhu, H.; Ou, H.; Popov, A. A New Phenomenological Constitutive Model for Thermoplastics. *Mech. Mater.* **2021**, *157*, 103817. [CrossRef]
26. Ferreira, B.P.; Carvalho Alves, A.F.; Andrade Pires, F.M. An Efficient Finite Strain Constitutive Model for Amorphous Thermoplastics: Fully Implicit Computational Implementation and Optimization-Based Parameter Calibration. *Comput. Struct.* **2023**, *281*, 107007. [CrossRef]
27. Xiang, Y.; Zhong, D.; Rudykh, S.; Zhou, H.; Qu, S.; Yang, W. A Review of Physically Based and Thermodynamically Based Constitutive Models for Soft Materials. *J. Appl. Mech.* **2020**, *87*, 110801. [CrossRef]
28. Ling, S.; Wu, Z.; Mei, J. Comparison and Review of Classical and Machine Learning-Based Constitutive Models for Polymers Used in Aeronautical Thermoplastic Composites. *Rev. Adv. Mater. Sci.* **2023**, *62*, 20230107. [CrossRef]
29. Duodu, E.A.; Gu, J.N.; Shang, Z.; Ding, W.; Tang, S. Damage Induced by High-Velocity Impact on Composite Structures Using Finite Element Simulation. *Iran. J. Sci. Technol. Trans. Mech. Eng.* **2017**, *41*, 97–107. [CrossRef]
30. Achour, N.; Chatzigeorgiou, G.; Meraghni, F.; Chemisky, Y.; Fitoussi, J. Implicit Implementation and Consistent Tangent Modulus of a Viscoplastic Model for Polymers. *Int. J. Mech. Sci.* **2015**, *103*, 297–305. [CrossRef]
31. Nahar, C.; Sanariya, S.; Gurralla, P.K. Numerical Simulation of Polymers at Low and Moderate Strain Rates. *Mater. Today Proc.* **2021**, *44*, 696–700. [CrossRef]
32. Yu, M.-H. Elasto-Plastic Constitutive Relations. In *Generalized Plasticity*; Springer: Berlin/Heidelberg, Germany, 2006; pp. 122–153. ISBN 978-3-540-25127-9.
33. Borja, R.I. J2 Plasticity. In *Plasticity*; Springer: Berlin/Heidelberg, Germany, 2013; pp. 31–58. ISBN 978-3-642-38546-9.
34. Taylor, G.I.; Quinney, H. The Latent Energy Remaining in a Metal after Cold Working. *Proc. R. Soc. Lond. Ser. Contain. Pap. Math. Phys. Character* **1934**, *143*, 307–326. [CrossRef]
35. Wilkins, M.L. *Calculation of Elastic-Plastic Flow*; University of California-Lawrence Radiation Laboratory: Livermore, CA, USA, 1963.
36. Maenchen, G.; Sack, S. *The Tensor Code*; University of California-Lawrence Radiation Laboratory: Livermore, CA, USA, 1963.
37. Simo, J.C.; Hughes, T.J.R. *Computational Inelasticity*; Interdisciplinary Applied Mathematics; Springer: New York, NY, USA, 1998; Volume 7, ISBN 978-0-387-97520-7.
38. Dunne, F.; Petrinic, N. *Introduction to Computational Plasticity*; Oxford University Press: Oxford, UK, 2005; ISBN 978-0-19-856826-1.
39. Zaera, R.; Fernández-Sáez, J. An Implicit Consistent Algorithm for the Integration of Thermoviscoplastic Constitutive Equations in Adiabatic Conditions and Finite Deformations. *Int. J. Solids Struct.* **2006**, *43*, 1594–1612. [CrossRef]
40. Ming, L.; Pantalé, O. An Efficient and Robust VUMAT Implementation of Elastoplastic Constitutive Laws in Abaqus/Explicit Finite Element Code. *Mech. Ind.* **2018**, *19*, 308. [CrossRef]
41. Ypma, T.J. Historical Development of the Newton–Raphson Method. *SIAM Rev.* **1995**, *37*, 531–551. [CrossRef]
42. Neto, M.A.; Ambrósio, J.A.C.; Leal, R.P. Sensitivity Analysis of Flexible Multibody Systems Using Composite Materials Components. *Int. J. Numer. Methods Eng.* **2009**, *77*, 386–413. [CrossRef]
43. Johnson, G.R.; Cook, W.H. A Constitutive Model and Data for Metals Subjected to Large Strains, High Strain Rates, and High Temperatures. In Proceedings of the 7th International Symposium on Ballistics, The Hague, The Netherlands, 19–21 April 1983; Volume 21, pp. 541–547.
44. Terselius, B.; Gedde, U.W.; Jansson, J.F. *Failure of Plastics: With 51 Tables*; Brostow, W., Corneliussen, R.D., Society of Plastics Engineers, Eds.; Hanser: München, Germany; Vienna, Austria; New York, NY, USA, 1986; ISBN 978-0-02-947510-2.
45. Brooks, J.W. Processing Wrought Nickel and Titanium Superalloys. In Proceedings of the Conference Organized in Celebration of the 75th Anniversary of the Swedish Society for Material Technology—Thermo-Mechanical Processing: Theory, Modelling and Practice, Stockholm, Sweden, 4–6 September 1996.
46. Duan, Y.; Saigal, A.; Greif, R.; Zimmerman, M.A. Analysis of Multiaxial Impact Behavior of Polymers. *Polym. Eng. Sci.* **2002**, *42*, 395–402. [CrossRef]
47. Dar, U.A.; Zhang, W. Polymer Based Aerospace Structures under High Velocity Impact Applications; Experimental, Constitutive and Finite Element Analysis. *J. Mech. Sci. Technol.* **2015**, *29*, 4259–4265. [CrossRef]
48. High-Velocity Impact of a Ceramic Target—SIMULIA User Assistance 2023. Available online: https://help.3ds.com/2023/english/dssimulia_established/simacaexarefmap/simaexa-c-impactceramictarget.htm?contextscope=all (accessed on 10 January 2024).

49. Mie, G. Zur Kinetischen Theorie Der Einatomigen Körper. *Ann. Phys.* **1903**, *316*, 657–697. [[CrossRef](#)]
50. Grüneisen, E. Theorie Des Festen Zustandes Einatomiger Elemente. *Ann. Phys.* **1912**, *344*, 257–306. [[CrossRef](#)]
51. Zhang, H.; Shukla, M.K.; Rajendran, A.M.; Jiang, S. Simulations of Single and Double Shock Experiments Using Generalized Interpolation Material Point Method with a Noise Control Strategy. *Comput. Part. Mech.* **2023**, *10*, 1795–1809. [[CrossRef](#)]
52. Johnson, G.R.; Holmquist, T.J. An Improved Computational Constitutive Model for Brittle Materials. *AIP Conf. Proc.* **1994**, *309*, 981–984.
53. Johnson, G.R.; Holmquist, T.J. Response of Boron Carbide Subjected to Large Strains, High Strain Rates, and High Pressures. *J. Appl. Phys.* **1999**, *85*, 8060–8073. [[CrossRef](#)]
54. Ramezani, M.; Ripin, Z.M.; Ahmad, R. Numerical Simulation of Sheet Stamping Process Using Flexible Punch. *Proc. Inst. Mech. Eng. Part B J. Eng. Manuf.* **2009**, *223*, 829–840. [[CrossRef](#)]
55. Ramezani, M.; Ripin, Z.M.; Ahmad, R. Plastic Bulging of Sheet Metals at High Strain Rates. *Int. J. Adv. Manuf. Technol.* **2010**, *48*, 847–858. [[CrossRef](#)]
56. Mooney, M. A Theory of Large Elastic Deformation. *J. Appl. Phys.* **1940**, *11*, 582–592. [[CrossRef](#)]
57. Doman, D.A.; Cronin, D.S.; Salisbury, C.P. Characterization of Polyurethane Rubber at High Deformation Rates. *Exp. Mech.* **2006**, *46*, 367–376. [[CrossRef](#)]
58. Mohotti, D.; Ali, M.; Ngo, T.; Lu, J.; Mendis, P. Strain Rate Dependent Constitutive Model for Predicting the Material Behaviour of Polyurea under High Strain Rate Tensile Loading. *Mater. Des.* **2014**, *53*, 830–837. [[CrossRef](#)]
59. Graff, K.F. *Wave Motion in Elastic Solids*; Dover Publications: New York, NY, USA, 1991; ISBN 978-0-486-66745-4.
60. Duan, Y.; Saigal, A.; Greif, R.; Zimmerman, M.A. Impact Behavior and Modeling of Engineering Polymers. *Polym. Eng. Sci.* **2003**, *43*, 112–124. [[CrossRef](#)]
61. El-Qoubaa, Z.; Colard, L.; Matadi Boumbimba, R.; Rusinek, A. Experimental Study and Modelling of Poly (Methyl Methacrylate) and Polycarbonate Compressive Behavior from Low to High Strain Rates. *J. Dyn. Behav. Mater.* **2018**, *4*, 179–189. [[CrossRef](#)]
62. Grujicic, M.; Bell, W.C.; Pandurangan, B.; He, T. Blast-Wave Impact-Mitigation Capability of Polyurea When Used as Helmet Suspension-Pad Material. *Mater. Des.* **2010**, *31*, 4050–4065. [[CrossRef](#)]
63. Derakhshani, S.M.; Schott, D.L.; Lodewijks, G. Micro–Macro Properties of Quartz Sand: Experimental Investigation and DEM Simulation. *Powder Technol.* **2015**, *269*, 127–138. [[CrossRef](#)]
64. Johnson, J.N. Dynamic Fracture and Spallation in Ductile Solids. *J. Appl. Phys.* **1981**, *52*, 2812–2825. [[CrossRef](#)]
65. Yaziv, D.; Bless, S.J.; Rosenberg, Z. Study of Spall and Recompaction of Ceramics Using a Double-impact Technique. *J. Appl. Phys.* **1985**, *58*, 3415–3418. [[CrossRef](#)]
66. Hawkins, M.C.; Thomas, S.A.; Fensin, S.J.; Jones, D.R.; Hixson, R.S. Spall and Subsequent Recompaction of Copper under Shock Loading. *J. Appl. Phys.* **2020**, *128*, 045902. [[CrossRef](#)]
67. Armanios, E.; Bucinell, R.; Wilson, D.; Chandra, N.; Chen, X.; Rajendran, A. The Effect of Material Heterogeneity on the Shock Response of Layered Systems in Plate Impact Tests. *J. Compos. Technol. Res.* **2002**, *24*, 232. [[CrossRef](#)]

Disclaimer/Publisher’s Note: The statements, opinions and data contained in all publications are solely those of the individual author(s) and contributor(s) and not of MDPI and/or the editor(s). MDPI and/or the editor(s) disclaim responsibility for any injury to people or property resulting from any ideas, methods, instructions or products referred to in the content.